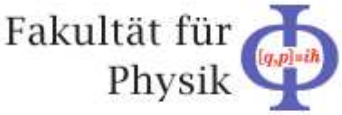

Bachelor's Thesis

Studien zu systematischen Unsicherheiten und Variablenwahlen in der Bestimmung der W-Helizität in Topereignissen

Studies of Systematic Uncertainties and Choice of Variables in Measurements of the W-Helicity in Top Events

prepared by

Chris Malena Delitzsch

from Hamburg

at the II. Institute of Physics

Thesis period:	12th April 2010 until 19th July 2010
Supervisor:	Dipl.-Phys. Andrea Knue Dr. Kevin Kröninger
First referee:	Prof. Dr. Arnulf Quadt
Second referee:	Prof. Dr. Ariane Frey
Thesis number:	II.Physik-UniGö-BSc-2010/03

Contents

1 Introduction

The Large Hadron Collider at CERN started running in November 2009 and is the world's largest particle accelerator. Protons are accelerated close to the speed of light and are brought to collision in order to investigate the interactions of their subcomponents. With these interactions, particle physicists hope to explore new energy scales. One hopes to find the Higgs boson, the only particle of the Standard Model which has escaped detection up to now and non-SM particles which are included in theories like Supersymmetry.
The heaviest particle of the Standard Model is the top quark with a mass close to that of a gold atom. Due to its large mass, the top quark decays after $\approx 5 \cdot 10^{-25}$ s almost exclusively into a W-boson and a bottom quark. Since this time is shorter than typical hadronisation times requires to form bound states, the top quark passes its polarization information onto its decay particles. The W-boson can be produced on-shell and has three different polarisation states. In this thesis studies leading towards a helicity measurement of the W-boson in semileptonic top pair decays with the Template Method is presented. The helicity fractions are determined with the transverse momentum of the charged lepton. The production of right-handed W-bosons is strongly suppressed in the SM. A deviation from the expected value could give a hint about non-SM couplings.

In Chapter 2, a short summary of the Standard Model of Particle Physics is given followed by an introduction to top quark physics. The production and decay mechanisms are presented as well as the background processes. Afterwards the helicity of the W-boson is discussed. The experimental setup of the LHC and the components of the ATLAS detector are described in Chapter 3. The signal and background samples used for this analysis are generated with Monte Carlo generators which are described in Chapter 4. This chapter introduces also the selection criteria for semileptonic $t\bar{t}$ events. Chapter 5 deals with the statistical tools which are crucial for the analysis. The reconstruction of the events via the Kinematic Likelihood Fit-

ter and the fitting procedure of the helicity fractions are explained. The results for the statistical und systematic uncertainties as well as a short comparison between two spin analysers are given in Chapter 6. Chapter 7 summarizes the studies and gives an outlook on further investigations.

2 Theoretical Overview

In this chapter, a short introduction into the Standard Model of Particle Physics and the production and decay of top quarks is given. An emphasis is placed on the helicity of the W-boson and the kinematic variables which allow its determination.

2.1 The Standard Model

The Standard Model of Particle Physics (SM) [1] is used to describe the elementary particles and their fundamental interactions. The expression *elementary* denotes particles without substructure. The SM contains fermions with spin s = $\frac{1}{2}$ and vector bosons with integer spin s = 1. The interactions between the fermions are mediated by these bosons.

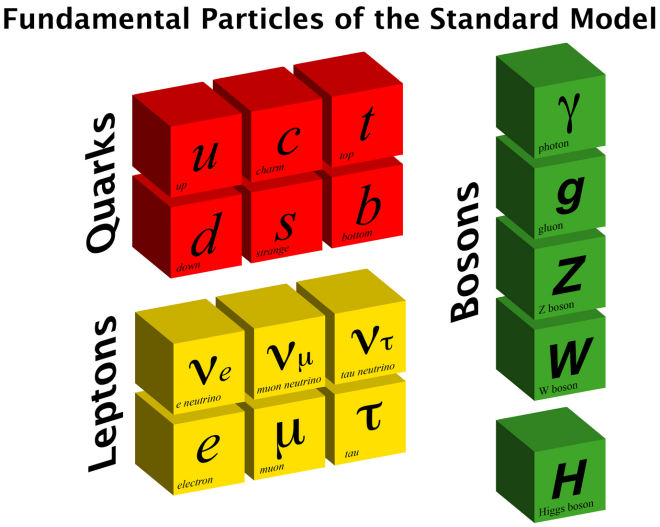

Figure 2.1: Elementary particles in the Standard Model.

The fermions are arranged into three generations each consisting of two weak isospin doublets. One doublet comprises an up-type quark with electric charge +$\frac{2}{3}$e and a down-type quark with -$\frac{1}{3}$e. The lepton doublet contains a charged lepton (q = -e)

and an electrically neutral neutrino, see Fig. 2.1. Each fermion has an antifermion with the same mass but opposite charge and weak isospin. The first generation contains the particles which are the building blocks of the visible matter. The up and down quark are the constituents of the proton (valence quarks) and form, together with the electrons, the atoms. The particles of the second and third generation have similar properties but much higher masses ($m_\tau = 1776.84 \pm 0.17$ MeV [2], $m_t = 173.1 \pm 0.6$ (stat.) $\pm$ 1.1 (syst.) $\frac{GeV}{c^2}$ [3]) and are therefore less stable. The Goldhaber experiment proved that the helicity of neutrinos is always left-handed if one neglects their small mass. Therefore leptons only exist in left-handed doublets and right-handed singlets. Compared to the leptons, the quarks have a further quantum number called colour (r, g, b). They do not exist as free particles but form colourless states, called hadrons (baryons and mesons).

The Standard Model includes three fundamental forces: the strong, the electromagnetic and the weak force. They are described by unitarity gauge groups SU(N) with N^2-1 gauge bosons, i.e that the Lagrangian is invariant under an SU(N)-transformation.
The strong force is described by the $SU(3)_C$ gauge group, also known as Quantum Chromo Dynamics. The mediators of this group are eight colour-charged massless gluons. Gluons do not carry electromagnetic charge and therefore couple only to quarks or to themselves.
The electromagnetic force is described by the U(1) gauge group consisting of phase transformations and causes interactions between charged particles. The electromagnetic force is mediated via massless photons. It therefore has an infinite range. The photons cannot couple to themselves because they do not carry electromagnetic charge.
The weak force can couple to all fermions and is described by three gauge fields. The force carriers are the massive $W^\pm$ and Z^0-bosons. Due to the large mass of the gauge bosons, the weak force has only a limited range and dominates only at high energies.
Glashow, Weinberg and Salam proposed in 1967 to unify the electromagnetic and the weak interaction to the electroweak interaction which is described by the group $SU(2)_L \otimes U(1)_Y$. The index L implies that the bosons couple exclusively to left-handed particles and the index Y represents the weak hypercharge. The electroweak force is mediated via four gauge bosons: the massless photon and the massive $W^\pm$

and Z^0-boson.

The symmetry group of the Standard Model is the combination of the electroweak and the strong interaction.

$$SU(3)_C \otimes SU(2)_L \otimes U(1)_Y$$

Interactions	Mediators	Relative strength	Range [m]
strong force	8 gluons	1	10^{-15}
electromagnetic force	photon	10^{-2}	∞
weak force	$W^{\pm}$, Z^0	10^{-13}	10^{-18}

Table 2.1: The three interactions of the Standard Model and their characteristic strength and range.

The Lagrangian in the Standard Model has to be invariant under local gauge transformations. The gauge bosons therefore have to be massless because mass terms would break the invariance. The discovery of the $W^{\pm}$ and Z^0 at the SPS collider at CERN showed that massive gauge bosons do exist. To include these masses into the Standard Model, the Higgs-Mechanism was introduced based on spontaneous symmetry breaking. In the Higgs-Mechanism, particles with higher masses have a stronger coupling to the Higgs-Field. A further particle has been predicted, the so-called *Higgs boson*. The Higgs boson is the only particle of the SM that has not been observed yet. The discovery of the Higgs particle is one of the most important research goals at the LHC.

Although the SM is a well-tested model, the theory is not complete because several aspects are not included. The SM contains only three of the four fundamental fources and does not describe the gravity. If the three interactions should be described by a *Grand Unified Theory*, their coupling constants have to be the same at the *grand unification scale* of approx 10^{16} GeV. Only about 4.6% of the Universe energy density is the baryonic matter comprising the particles of the SM, about 95% of the Universe energy density is dark matter and energy which is not described by the SM. Furthermore the source of the matter-antimatter asymmetry is an unanswered question in the SM. The CP violation in the weak interaction could be an explanation for the disappearance of the antimatter but the effects observed so far

are too small.

2.2 The Top Quark

Although the top quark has been predicted much earlier in 1977 as the weak isospin partner of the b-quark, it was only discovered in 1995 at the Tevatron collider at Fermilab (Chicago) [4, 5]. It is the heaviest known elementary particle. The top quark's mass is the most precise measured quark mass and its current world average is $173.3 \pm 1.1 \frac{\text{GeV}}{\text{c}^2}$ [3]. Having a mass close to the scale of electroweak symmetry breaking (EWSB), the top quark will play an important role for searches of physics beyond the SM.

2.2.1 Top Pair Production

At hadron colliders top quark pairs are produced either by quark-antiquark annihilation or by gluon-gluon-fusion via the strong interaction. The leading order Feynman diagrams are depicted in Fig. 2.2.

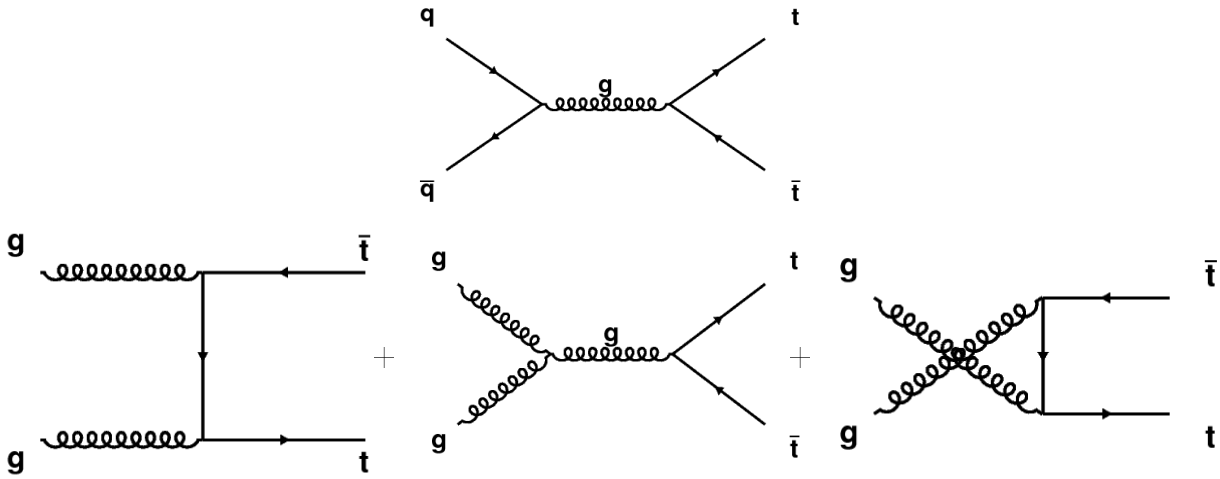

Figure 2.2: Leading order Feynman diagrams for the $t\bar{t}$ production via quark-antiquark annihilation (upper plot) and gluon-gluon fusion (lower plot).

The cross sections for the $t\bar{t}$ production at the Tevatron [6] and the LHC [7] are calculated to be, respectively:

$$\begin{aligned} \sigma_{t\bar{t}} &= 7.39 \pm^{0.57}_{0.52} \text{ pb} && \text{assuming } m_{\text{t}} = 172.0 \text{ GeV/c}^2, \sqrt{s} = 1.96\text{TeV} \\ \sigma_{t\bar{t}} &= 401.6 \text{ pb} \pm^{3.6\%}_{4.3\%} \pm^{4.6\%}_{4.5\%} && \text{assuming } m_{\text{t}} = 172.5 \text{ GeV/c}^2, \sqrt{s} = 10 \text{ TeV} . \end{aligned}$$

As a result of the pertubative QCD at high energies these processes can be described by the interaction of quarks and gluons which are the constituents of the colliding hadrons. The quarks and gluons carry only a fraction x of the proton momentum, the so-called Bjorken x. Due to the smaller momentum of the partons, the center-of-mass energy of an interaction between two partons i and j is smaller: $\sqrt{\hat{s}} = \sqrt{x_\mathrm{i} x_\mathrm{j} s}$. To produce a $t\bar{t}$-pair the effective center-of-mass energy, $\sqrt{\hat{s}}$, has to be large enough to produce the top quark pair at rest:

$$\sqrt{x_\mathrm{i} x_\mathrm{j} s} \geq 2m_\mathrm{t} \ . \tag{2.1}$$

Assuming that $x_\mathrm{i} \approx x_\mathrm{i} = x$, it follows:

$$x \ = \ \frac{2m_\mathrm{t}}{\sqrt{s}} \ . \tag{2.2}$$

At the Tevatron the center-of-mass energy is $\sqrt{s} = 1.96$ TeV whereas the aimed center-of-mass energy of the Large Hadron Collider is $\sqrt{s} = 14$ TeV.

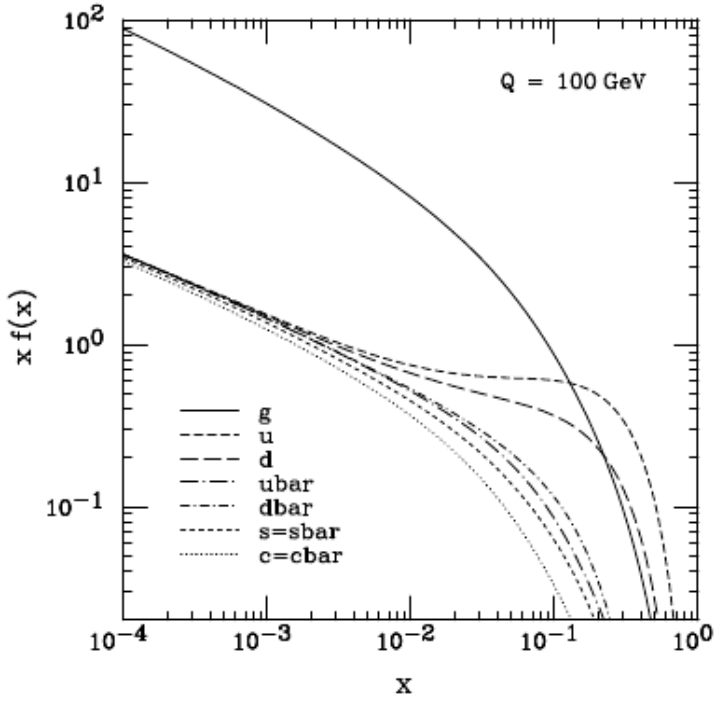

Figure 2.3: Parton distribution functions for Q = 100 GeV from the CTEQ collaboration [8].

To produce a $t\bar{t}$ pair at the Tevatron one needs a much larger proton momentum

fraction x. The Parton Density Functions (PDFs) give the probability density for a quark or gluon with a certain momentum fraction x to be in the proton at an energy scale of Q^2.
For large values of x the distribution for the up- and down-quark dominates over the gluons, see Fig.(2.3). Therefore the top pair production by quark-antiquark annihilation dominates at the Tevatron (85%) whereas the gluon-gluon fusion is the dominating process at the LHC (90%) at 14 TeV. Tab. 2.2 contains the values for the proton momentum fractions x at threshold depending on the center-of-mass energy according to formula 2.2.

Center-of-mass energy $\sqrt{s}$	1.96 TeV	7 TeV	10 TeV	14 TeV
Min. Bjorken x	0.177	0.049	0.035	0.025

Table 2.2: Bjorken x for different center-of-mass energies at the Tevatron (1.96 TeV) and the Large Hadron Collider (7, 10, 14 TeV).

2.2.2 Single Top Production

Single top quarks were discovered in 2009 at the Tevatron [9, 10]. They are produced via the weak interaction in three different channels. The leading order Feynman diagrams are shown in Fig. (2.4).

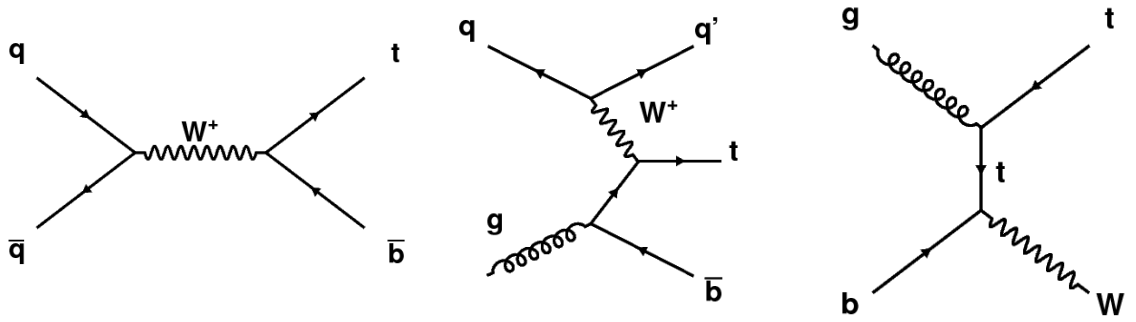

Figure 2.4: Feynman diagrams for the single top quark production in the s-channel (left), t-channel (middle) and the associated Wt production (right)

The single top production can be used for the direct measurement of the CKM matrix element $|V_{tb}|^2$ which was unmeasured before. Furthermore the single top production will be used to study the spin of the top quark [11]. The NNLO (s-channel, Wt production) and NLO (t-channel) cross section for the single top production are shown in Tab. 2.3.

channel	σ [pb] @ Tevatron	σ [pb] @ LHC
s-channel	$0.523\ \pm^{0.001}_{0.005}\pm^{0.030}_{0.028}$	$5.16\ \pm^{0.09}_{0.09}\pm^{0.20}_{0.14}$
t-channel	$0.981\ \pm^{0.023}_{0.003}\pm^{0.098}_{0.082}$	$83.5\ \pm^{1.40}_{1.10}\pm^{1.50}_{1.70}$
Wt production	≈ 0	$19.4\ \pm^{0.50}_{0.50}\pm^{1.00}_{1.10}$

Table 2.3: Cross section for the single top production at the Tevatron $\sqrt{s} = 1.96$ TeV and the LHC $\sqrt{s} = 10$ TeV. The calculations are based on a top mass of $m_t = 173\ \mathrm{GeV/c^2}$ [12] for the s-channel and Wt production. The cross section for the t-channel for the top production is based on a top mass of $m_t = 172\ \mathrm{GeV/c^2}$ [13]. The current world average top mass is $173.3 \pm 1.1\ \frac{\mathrm{GeV}}{\mathrm{c^2}}$

2.2.3 Top Quark Decay

Due to its large mass, the top quark has a short lifetime [14] of :

$$\tau_t = \frac{1}{\Gamma_t} \approx 5 \cdot 10^{-25}\ \mathrm{s},$$

where Γ_t is the decay width of the top quark. The hadronisation time depends on the QCD timescale [15, 16]:

$$\tau_{\mathrm{had}} = \frac{1}{\Lambda_{\mathrm{QCD}}} \approx 3 \cdot 10^{-24}\ \mathrm{s}\ .$$

Therefore, the top quark decays via the weak interaction before it can hadronise. The CKM matrix predicts that the top quark decays almost exclusively into a W-boson and a bottom quark with $|V_{\mathrm{tb}}| = 0.999152^{+0.000030}_{-0.000045}$ [17].
While the b-quark hadronises to a jet, the W-boson can either decay leptonically into a charged lepton and its corresponding anti-neutrino (branching ratio BR $\approx$ 33.3% [18]) or hadronically into two quarks (BR $\approx$ 67.7% [18]). Neutrinos only take part in the weak interaction and can therefore not be directly observed in the detector. While they carry a certain fraction of the total momentum, one can detect them by measuring the missing transverse energy.

According to their final state particles, $t\bar{t}$-events are divided into three different channels:

- **dileptonic**:
  Both W-bosons decay leptonically. The branching ratio BR for the decay in either electrons or muons is BR= $\frac{4}{81} \approx 4.94\%$. The signal consists of two jets

from the b-quarks, two charged leptons with a high transverse momentum p_{T} and two neutrinos which can be observed as missing transverse energy $E_{T_{miss}}$. Having two neutrinos in the final state, it is not possible to fully reconstruct the $t\bar{t}$ events. The dileptonic decay channel has only small background contributions.

- **semileptonic**:
  In the semileptonic channel, one W-boson decays leptonically while the other decays hadronically. The signature consists of four jets, one high p_{T} lepton and missing transverse energy. Compared to the dileptonic channel, the branching ratio of the semileptonic decay into electrons or into taus decaying into electrons, BR= 0.1725%, is larger but at the same time the background increases due to QCD multijet production and combinatorial background. Nevertheless, this channel has a good signal to background ratio and is therefore called *golden channel* although the classification of the jets to the bottom quarks and the light-quarks of the hadronic W-decay is very difficult.

- **all-jets**: In the all-jets channel, both W-bosons decay hadronically. This signal has the largest BR $= \frac{36}{81} \approx 44.44\%$. It suffers from large background contributions due to QCD multijet production and combinatorial background.

The semileptonic decay channel will be assumed in the following studies.

2.2.4 Background Processes

Background processes are events with the same signature as the signal. Possible background processes for the semileptonic decay channel of $t\bar{t}$ pairs are W + jets, Z+jets, single top events, the dileptonic and all-jets decay channel and QCD multijet events, in which a lepton and $E_{T_{miss}}$ are faked (further background processes, see Chapter 4.2).
In W + jet events, the W-boson decays into an electron, a muon or a tau and its corresponding neutrino. Additional jets are produced via initial or final state radiation as well as from underlying events.
The Z-boson in Z + jets events decays into lepton-antilepton pairs while one of the leptons is not detected and can be measured as missing transverse energy. The dileptonic decay channel has to be considered as background because one lepton may not be detected. The QCD multijet background consists of leptons with fake

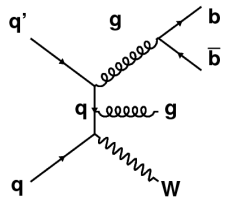

Figure 2.5: Background event with W + 3jets. One gluon decays into a $b\bar{b}$ - pair and the third jet comes from the radiation of one gluon.

isolation and additional jets.
The processes W + jets and the dileptonic decay channel contribute the most to the background of $t\bar{t}$ pairs. In order to get a good signal over background ratio the background has to be reduced. Therefore a proper object definition and event selection is crucial and will be discussed in Chapter 4.

2.3 Helicity of the W-Boson

The helicity of a particle is defined as the projection of the spin $\vec{s}$ onto the momentum direction $\vec{p}$, i.e,

$$h = \frac{\vec{s} \cdot \vec{p}}{|\vec{s}| \cdot |\vec{p}|} \ . \tag{2.3}$$

The large top quark mass allows for real W-boson production with different helicity states. Having integer spin of one, the following helicity states are possible:

- **right-handed: h = +1**
  If the W-boson is right-handed, the spin points in the direction of the momentum.
- **left-handed: h = -1**
  The spin of a left-handed W-boson points in opposite momentum direction.
- **longitudinal polarised: h = 0**
  If the spin direction is perpendicular to the direction of momentum, the W-boson is called longitudinal polarised.

The Wtb-vertex of the weak interaction has a vector-axial vector structure (V-A):

$$-i\frac{g}{\sqrt{2}}V_{q_i q_j}\gamma^{\mu}(1-\gamma^5) \ .$$

Therefore the W-boson can only couple to left-handed fermions. The SM predicts that the top quark has the V-A coupling like all the other fermions.
Assuming that the mass of the bottom quark is zero in comparison to the W-boson mass and the top quark mass, the helicity of the bottom quark has to be left-handed. If the W-boson were right-handed the spin along the momentum axis would be $+\frac{3}{2}$ which disagrees with the assumption of the top quark spin to $\frac{1}{2}$ (see Fig. 2.6). This implies that the Standard Model prediction for right-handed W-bosons in the top decay is zero.

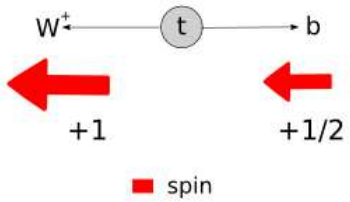

Figure 2.6: Illustration of the right-handed W-boson suppression.

The fraction of longitudinal polarised W-bosons is defined as:

$$\begin{aligned} F_0 &= \frac{\Gamma(t \to W_{long} + b)}{\Gamma(t \to W_{long} + b) + \Gamma(t \to W_- + b) + \Gamma(t \to W_+ + b)} \\ &= \frac{\left(1 - \left(\frac{m_b}{m_t}\right)^2\right)^2 - \left(\frac{m_W}{m_t}\right)^2 \left(1 + \left(\frac{m_b}{m_t}\right)^2\right)}{\left(1 - \left(\frac{m_b}{m_t}\right)^2\right)^2 + \left(\frac{m_W}{m_t}\right)^2 \left(1 - 2\left(\frac{m_W}{m_t}\right)^2 + \left(\frac{m_b}{m_t}\right)^2\right)} . \end{aligned}$$

where m_b is the mass of the bottom quark, m_t is the mass of the top quark and m_w the mass of the W-boson. The definition of the left- and right-handed fraction is analogue. Neglecting terms at the order of $\left(\frac{m_b}{m_t}\right)^2$ leads to:

$$\begin{aligned} F_0 &\approx \frac{m_t^2}{2m_w^2 + m_t^2} \approx 0.699 , \\ F_- &\approx \frac{2m_w^2}{2m_w^2 + m_t^2} \approx 0.301 , \\ F_+ &= 0. \end{aligned}$$

with $\mathrm{m_t} = 173.1\ \frac{\mathrm{GeV}}{\mathrm{c}^2}$ and $\mathrm{m_W} = 80.399\ \frac{\mathrm{GeV}}{\mathrm{c}^2}$ [19]. Taking the small mass of the bottom quark into account, the prediction of the SM for the right-handed polarisation yields:

$F_+ = 3.6 \cdot 10^{-4}$ [20].

2.3.1 Measurements

The helicity of the W-boson has been measured at the Tevatron by the DØ [21] and the CDF [22] Collaborations. The result for the longitudinal helicity fraction measurement are:

$$\begin{aligned} F_0^{DO} &= 0.490 \pm 0.106 \text{ (stat.)} \pm 0.085 \text{ (syst.)} , \\ F_0^{CDF} &= 0.637 \pm 0.084 \text{ (stat.)} \pm 0.069 \text{ (syst.)} \end{aligned}$$

The measurements are based on a data sample of 2.7 fb^{-1} (DØ) and 1.9 fb^{-1} (CDF). While the DØ collaboration measured only the fractions F_0 and F_+ and fixed the left-handed fraction according to $F_0 + F_- + F_+ = 1$, the CDF collaboration fixed the right-handed fraction to its expectation value in the Standard Model $\text{F}_+ \approx 0$.

2.3.2 Spin Analyser

For the studies of the W-boson helicity different analysers are used which will be presented in this chapter. Each analyser has different distributions for the three possible helicity states.

The angular variable $\cos\theta^*$

The variable $\cos\theta^*$ (helicity angle) is a common variable for W-helicity studies. The angle θ^* is defined as the angle between the charged lepton in the rest frame of the W and the W-boson in the rest frame of the top quark, see Fig 2.7.
In the SM the distributions for the different helicity states are defined as:

$$\begin{aligned} \frac{1}{\text{N}}\frac{\text{dN}}{\text{d}\cos\theta^*} &= \frac{3}{8}(1-\cos\theta^*)^2 \cdot F_- + \frac{3}{8}(1+\cos\theta^*)^2 \cdot F_+ + \frac{3}{4}(\sin^2\theta^*) \cdot F_0 \\ &= \omega_- + \omega_+ + \omega_0 \ . \end{aligned}$$

Integration over the variable $\cos\theta^*$ in the interval [-1:1] leads to:

$$1 = F_- + F_+ + F_0 \ .$$

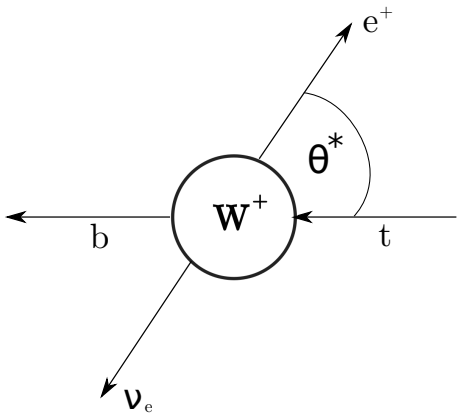

Figure 2.7: Definition of the angle θ^*.

This normalisation allows the third helicity fraction to be determined if the other two are known.
Fig. (2.8) shows the distributions for the three helicity states assuming the Standard Model fractions of F_0=0.699, F_-=0.301 (for W^+) und F_+=0.301 (for W^-). The solid line shows the Standard Model prediction for a W^+ boson.

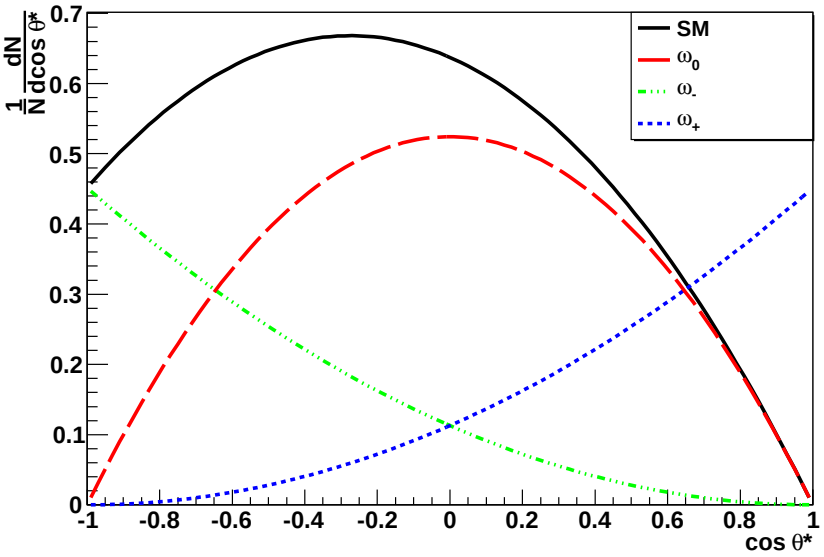

Figure 2.8: Helicity angle distributions of the different helicity states. The solid line shows the distribution according to the Standard Model, the dashed line represents the longitudinal helicity, the dashed-dotted line the left-handed helicity and the dotted line the right-handed helicity.

Invariant Mass m^2_{lb}

Another way to determine the helicity fractions is to use the squared of the invariant mass of the charged lepton and the b-quark, m^2_{lb} [23]. This variable is connected to the spin analyser $\cos\theta^*$:

$$\begin{aligned} m^2_{lb} &= (p_l + p_b)^2 \\ &= (E_l + E_b)^2 - (\vec{p_l} + \vec{p_b})^2 \\ &= 2E_l E_b(1 - \cos\theta_{lb}) \\ &\approx 2E_l E_b(1 + \cos\theta^*) \\ \Longrightarrow \cos\theta^* &\approx \frac{m^2_{lb}}{2E_l E_b} - 1 \end{aligned}$$

p_T of the charged lepton

The third spin analyser is the transverse momentum of the charged lepton. This variable will be used in the following studies. The transverse momentum of the charged lepton is a kinematic variable which can be measured very precisely. Furthermore it is barely influenced by the jet energy scale (JES) (for further information see Chapter 6.5.2). One advantage of the transverse momentum is the use in the dileptonic channel where the helicity fractions can be calculated for both decaying W-bosons. Fig. 2.9 shows the leptonic decay of the W-boson for the different helicity states.

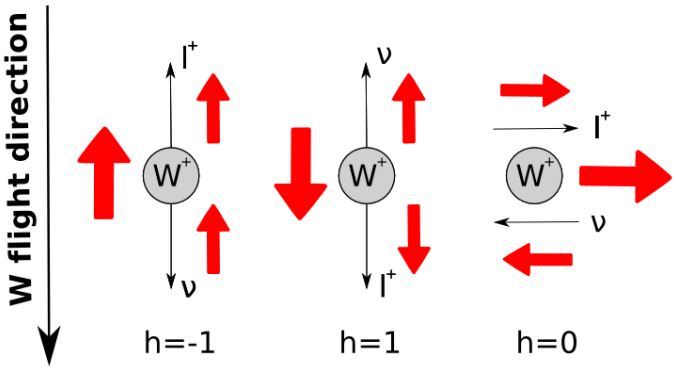

Figure 2.9: Helicity of the leptonically decaying W-boson.

In case of a left-handed W-boson the charged lepton is emitted against the flight direction of the W-boson. In contrast to that the right-handed W-boson emits the charged lepton into the flight direction. Therefore the lepton resulting of a decay of

a right-handed W-boson has a higher transverse momentum compared to a lepton of a left-handed W-boson.

3 Experimental Setup

This chapter deals with the Large Hadron Collider and its detectors. The ATLAS detector and its components are introduced.

3.1 The Large Hadron Collider

The Large Hadron Collider (LHC) is a proton-proton collider located at CERN, Geneva. The beam pipe is situated in the previous LEP tunnel and has a circumference of 27 km. The LHC is designed to have a center-of-mass energy of $\sqrt{s} = 14$ TeV and a luminosity of $\mathcal{L} = 10^{34}$ cm^{-2}s^{-1}. Until the end of 2011 the LHC runs at a center-of-mass energy of 7 TeV.

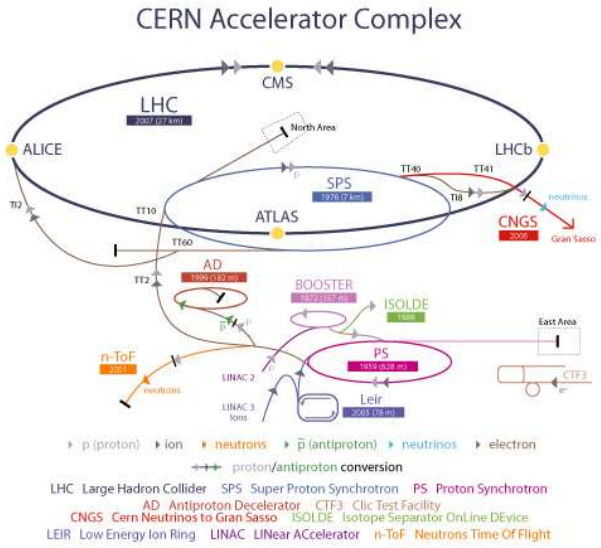

Figure 3.1: The LHC accelerator and its pre-accelerators [24].

Before being injected into the LHC ring, the protons are preaccelerated in the linear accelerator LINAC2 and several ring accelerators like the PS and SPS [25]. After an acceleration to 450 GeV in the SPS, the proton bunches are transferred to the LHC circulating 20 minutes to achieve the design center-of-mass energy, see Fig. 3.1. Each

proton beam consists of 2,808 bunches with $1.15{\cdot}10^{11}$ protons per bunch [26]. At the LHC the number of collisions is supposed to be approximately 40 million per second.

The four main experiments of the LHC are ALICE, ATLAS, CMS and LHCb. ALICE (A Large Ion Collider Experiment) investigates lead ion collisions which create quark-gluon plasma. LHCb is an experiment to study b-physics in order to investigate the matter-antimatter asymmetry. CMS (Compact Muon Solenoid) and ATLAS (A Toroidal LHC Apparatus) belong to the general-purpose detectors. Both experiments have a wide range of physics topics they want to investigate. Although both experiments have the same physical goal, the technical design of their detector components is different.

3.2 The ATLAS Detector

The ATLAS detector is a general-purpose detector and has a typical onion-shell structure. The detector is forward-backward symmetric with respect to the interaction point and has a total length of 44 m and a weight of approximately 7,000 t [27]. ATLAS comprises four major parts: the inner detector, the electromagnetic and hadronic calorimeter, the muon spectrometer and the magnet system whereas the magnet system is divided into the solenoidal and toroidal magnets.

3.2.1 Detector Coordinates

The coordinate system of ATLAS is right-handed with the origin placed in the interaction point and the z-axis pointing along the beam-pipe. The x-coordinate points towards the center of the LHC and the y-coordinate upwards. The azimuthal angle ϕ in the xy-plane is defined as:

$$\phi = \arctan\left(\frac{y}{x}\right) \ ,$$

and the polar angle θ is the angle between the momentum of the particle and the beam-axis. Instead of localizing a particle by its coordinates in the xyz-coordinate system, the pseudo-rapidity is introduced:

$$\eta = -\ln\left(\tan\left(\frac{\theta}{2}\right)\right) \ .$$

The advantage of using this parameter is the invariance of $\Delta\eta$ under Lorentz boosts along the beam axis.
To determine the distance of particles, ΔR is measured in the calorimeters:

$$\Delta R = \sqrt{\Delta\eta^2 + \Delta\phi^2} \ .$$

The transverse momentum of a particle is defined as the momentum in the plane perpendicular to the beam pipe:

$$p_{\mathrm{T}} = \sqrt{p_{\mathrm{x}}^2 + p_{\mathrm{y}}^2} \ .$$

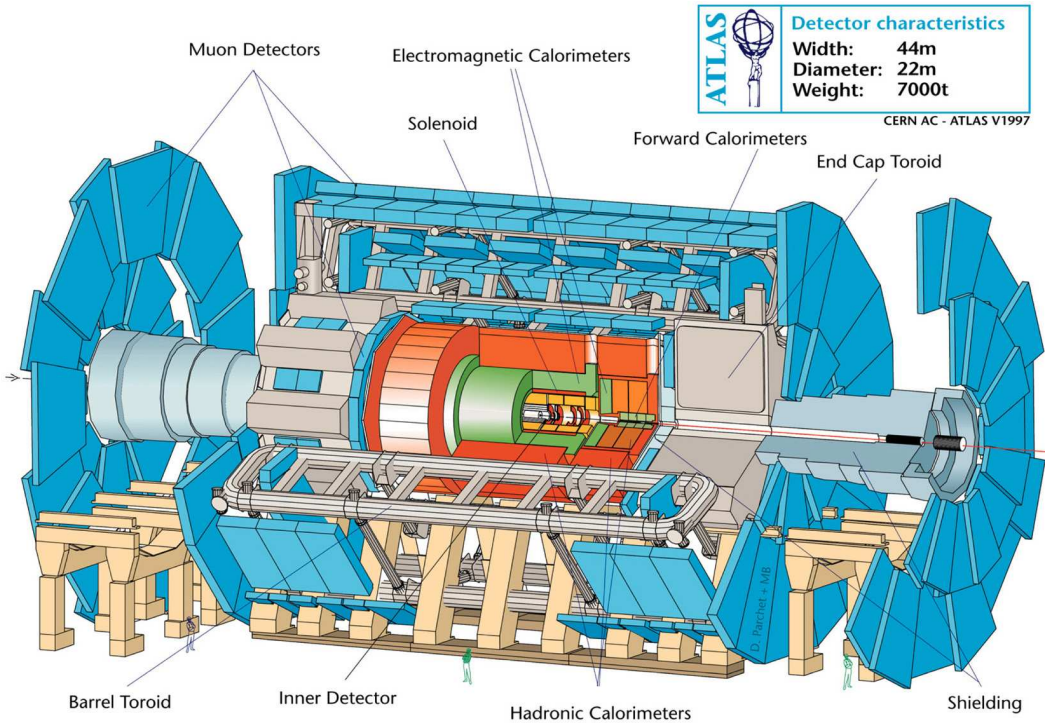

Figure 3.2: The ATLAS experiment.

3.2.2 The Inner Detector

The innermost part of the detector which is surrounded by a 2 T solenoidal magnet contains the *Pixel Detector, the Semiconductor Tracker (SCT)* and the *Transition Radiation Tracker (TRT)* [28]. The Pixel Detector consists of three layers in the

barrel and three discs at each endcap with 80.4 million pixels. The innermost layer is installed with a distance of 50.5 mm to the beam. The pixel detector has therefore to be made of material which is radiation hard. After a few years running, a new B-layer will be installed. The SCT consists of eight layers of silicon microstrip detectors to afford eight measurements of (R, Φ) for each track . Furthermore the impact parameter and the vertex position can be determined by the SCT. The TRT consists of straw tubes which are filled with a gas mixture of 70% Xenon gas, 27% CO_2 and 3% O_2. If an electron or charged pion traverses a region with different dielectric constants, the particle radiates photons which ionize the gas. The drift time of the particles is read out by 420,000 channels providing a partial resolution of the particle track of 170 μm.

3.2.3 Calorimeters and Energy Resolution

The calorimeters are divided into the *electromagnetic* and the *hadronic calorimeter*. Both calorimeters are sampling calorimeters consisting of passive absorber material and active material. The calorimeters are used to measure the energy of particles like electrons, hadrons and photons. If a particle enters the calorimeter, it interacts with the passive absorber material and secondary particles are produced via bremsstrahlung and pair production. Further e^+e^- pairs are produced in showers whose number of particles N depends on the initial energy E of the incoming particle. The number of produced particles follows Poisson statistics. Therefore the energy resolution of the calorimeter is defined as:

$$\frac{\sigma_E}{E} \propto \frac{a}{\sqrt{E}},$$

where a describes statistical fluctuations in the shower. Furthermore, the systematic uncertainties like miscalibration of the detector have to be taken into account via the constant factor b as well as the noise described by the factor c. The energy resolution is parametrised as

$$\frac{\sigma_E}{E} = \frac{a}{\sqrt{E}} \oplus b \oplus \frac{c}{E}$$

and is dominated by the contributions of statistical fluctuations.
The electromagnetic calorimeter (ECal) uses lead as passive absorber material due to its high density and liquid Argon as active material. Furthermore, it is divided

into a barrel region and two end-caps. The resolution of the ECal is:

$$\frac{\sigma_{\mathrm{E}}}{E} = \frac{10\%}{\sqrt{E}} \oplus 0.7\% \ .$$

The hadronic calorimeter is divided into the tile calorimeter, the liquid Argon forward- and end-cap calorimeter. The tile calorimeter encloses the electromagnetic calorimeter and uses steel as passive absorber and scintillating tiles as active material. The resolution of the hadronic barrel and the endcaps is

$$\frac{\sigma_{\mathrm{E}}}{\sqrt{E}} = \frac{50\%}{\sqrt{E}} \oplus 3\% \ ,$$

while the resolution of the hadronic forward calorimeter is:

$$\frac{\sigma_{\mathrm{E}}}{\sqrt{E}} = \frac{100\%}{\sqrt{E}} \oplus 10\% \ .$$

3.2.4 The Muon Spectrometer

The momentum of the muons is measured in the *muon spectrometer* which is the outer part of the ATLAS detector. The muon spectrometer consists of a toroidal magnetic field and four different types of detectors: the Monitored Drift Tubes, Cathode Strip Chambers and the trigger chambers: Resistive Plate Chambers and Thin Gap Chambers. In order to determine the transverse momentum of the muon, the sagitta s is measured:

$$p_{\mathrm{T}} = \frac{s^2 + \frac{d^2}{4}}{2s} \ q \ B$$

where d is the chord and B the magnetic field. The relative resolution of the transverse momentum is:

$$\frac{\sigma_{\mathrm{T}}}{p_{\mathrm{T}}} \propto p_{\mathrm{T}} \ ,$$

and for the muon system @ $\mathrm{p_T} = 1$ TeV:

$$\frac{\sigma_{\mathrm{T}}}{p_{\mathrm{T}}} = 10\% \ .$$

3.2.5 Trigger System

Due to the high luminosity, one expects a huge amount of data per collision. About 40 MHz of data has to be reduced to about 200 Hz which will be stored. The data reduction is performed by a three level trigger system. The system consists of the level 1 trigger which is hardware based and the level 2 trigger and the event filter which are large computing farms.

4 Monte Carlo Samples

In this chapter the Monte Carlo generators for the used data sets in the analysis are presented and the used background samples are described. Furthermore the selection criteria for semileptonically decaying $t\bar{t}$ events are introduced.

4.1 Signal Events

The data sets used in the following studies are generated via the leading-order Monte Carlo generator PROTOS (PROgram for TOp Simulations)[29]. PROTOS allows for generation of single top and top pair events including flavour changing neutral currents and anomalous Wtb couplings.

PROTOS includes the most general Wtb vertex:

$$\mathcal{L}_{\mathrm{Wtb}} = -\frac{g}{\sqrt{2}}\ \bar{b}\ \gamma^{\mu}(V_{\mathrm{L}}P_{\mathrm{L}} + V_{\mathrm{R}}P_{\mathrm{R}})\ t\ W_{\mu}^{-} - \frac{g}{\sqrt{2}}\ \bar{b}\ \frac{i\sigma^{\mu\nu}q_{\nu}}{M_{\mathrm{W}}}(g_{\mathrm{L}}\ P_{\mathrm{L}} +\ g_{\mathrm{R}}P_{\mathrm{R}})\ t\ W_{\mu}^{-} + h.c$$

with the four couplings V_{R}, V_{L}, g_{R}, g_{L}. The couplings are assumed to be real and depend on the top quark mass. In the Standard Model prediction the four couplings are: $V_{\mathrm{R}} = g_{\mathrm{R}} = g_{\mathrm{L}} = 0$ and $V_{\mathrm{L}} = 1$. One option of the generator is to fix the helicity of the W-boson in the process $t \to Wb$ to the values -1, 0 or 1.
The samples to create the three templates are generated with a determined W-helicity of $F_0 = 1$, $F_{\text{-}} = 1$ and $F_{+} = 1$. One data set is generated with helicity fractions according to the SM expectation. Each data set is produced at a center-of-mass energy of $\sqrt{s} = 10$ TeV and a top quark mass of $m_{\mathrm{t}} = 172.5\ \frac{\mathrm{GeV}}{c^2}$.

The detector simulation of the generated events has been performed by GEANT4 [30] and the reconstruction with the ATLAS offline software ATHENA.

4.2 Background Events

Tab. 4.1 summarises the generated background processes and the used Monte Carlo generators. Moreover the table lists the used showering algorithm and the cross section. The W+jets and Z+jets events are generated with Alpgen which is a leading

Table 4.1: For each generated background sample, the used Monte Carlo Generator and showering algorithm is indicated. The right column contains the cross-section.

Background process	MC Generator	Showering	Cross section [pb]
Fully hadronic	MCatNLO	Jimmy	182.69
Dilepton	Protos	Pythia	42.16
Hadronic dec. τ	Protos	Pythia	37.20
Single Top (Wt)	AcerMC		14.13
Single Top (t-channel)	AcerMC		43.18
Single Top (s-channel)	AcerMC		2.76
W (eν) + jets	Alpgen	Jimmy	16163.78
W ($\mu\nu$) + jets	Alpgen	Jimmy	16149.51
W ($\tau\nu$) + jets	Alpgen	Jimmy	16144.26
Z (ee) + jets	Alpgen	Jimmy	1471.45
Z ($\mu\mu$) + jets	Alpgen	Jimmy	1469.10
Z ($\tau\tau$) + jets	Alpgen	Jimmy	1477.36
Wbb + jets	Alpgen	Jimmy	17.86
Diboson	Herwig		37.14

order Monte Carlo generator for hard multiparton processes in hadronic collisions [31]. Single top events were produced with AcerMC which is specialised on the generation of SM background processes at the LHC [32]. The full hadronically decaying $t\bar{t}$ pairs are generated with the next-to-leading order generator MC@NLO [33]. For the single top samples of AcerMC and for all MC@NLO samples one has to take into account that the generated events can also have a negative weight. This effects the kinematical distributions and the calculation of the total cross section for the samples.

4.3 Object Definition

In order to identify the particles which enter the detector, object definitions are introduced which depend on the quantities measured in the detector components. A particle is defined as a "good/well" reconstructed electron if it fulfills the following object definitions:

- the particle has to shower in the electromagnetic calorimeter,
- the transverse momentum p_T has to be larger than 20 GeV/c,
- the pseudorapidity is constrained to $|\eta| < 2.47$,
- Etcone20 $<$ 40 GeV + 0.023 Et: the transverse energy in a cone with a radius of 0.2 is smaller than 4.0 GeV and a small fraction of the transverse energy.
- The crack region is excluded.

If a particle is detected as a "good/well" reconstructed muon, it has passed the selection criteria:

- the transverse momentum p_T has to be larger than 20 GeV/c.
- The additional transverse momentum deposited in a cone of $\Delta R < 0.3$ around the muon has to be smaller than 4 GeV.
- The pseudorapidity is constrained to $|\eta| < 2.47$.
- The ratio of the transverse energy to the transverse momentum reaches maximally the value 0.1.
- To make sure, that the muon is not emitted from a jet, the ΔR distance between jet and muon has to be larger than 0.3. Furthermore, the ratio of the transverse jet-energy to the transverse muon momentum is only allowed to be smaller than 0.5.

A jet has to have at least a transverse momentum of 20 GeV/c and has to be in a region of $|\eta| < 2.5$. A lepton can be identified as a jet and is entering the jet-container during the reconstruction. To avoid double-counting, all jets within a cone of 0.2 around a good reconstructed electron are removed.

4.4 Event Selection

Due to the limited time available for a Bachelor thesis, only semileptonic $t\bar{t}$ events which have an electron in the final state (e+jets)are considered. Events which are taken into account for the semileptonic decay of $t\bar{t}$ pairs have to fulfill several selection criteria. For the generation of the template distributions also the leptonically decaying τ-leptons are taken into account. Therefore all hadronically decaying τ are cut out in the pre-selection cut. The remaining events have to require the following cuts which have been used within the ATLAS cross section group [28].

4.4.1 Selection Criteria

The selection criteria are:

1. Exactly one reconstructed triggered electron with $\mathrm{p_T} > 20$ GeV/c and $|\eta| < 2.5$ and exactly zero muons,

2. $E_{\mathrm{T}}^{\mathrm{miss}} > 20$ GeV,

3. at least three anti-$\mathrm{k_t}$ jets with $\mathrm{p_T} > 40$ GeV/c and $|\eta| < 2.5$,

4. at least one additional anti-$\mathrm{k_t}$ jet with $\mathrm{p_T} > 20$ GeV/c and $|\eta| < 2.5$.

4.4.2 Selection Efficiencies

Tab.4.2 and 4.3 summarize the remaining number of events after applying the different cuts for the longitudinal, left-handed and right-handed template as well as the Standard Model data set. Apart from the described cuts a further criterion is introduced. Only leptons with a transverse momentum smaller than 200 GeV/c are considered. Looking at the Standard Model distribution in Fig. 6.1 one can see that several bins with a $\mathrm{p_T}$ larger than 200 GeV/c have no entries. For the ensemble tests which are described in Chapter 5.3, the bins must comprise non-zero entries to allow for the determination of the helicity fractions. In order not to loose statistics, one could also fill all events with $\mathrm{p_T}$ larger than 200 GeV/c into one overflow bin. This procedure has not been applied in this Bachelor thesis but should be considered for further studies. Furthermore the efficiency of the selected events compared to the amount of pre-selected events is indicated. The errors of the efficiencies are

binominal:

$$\sigma(\varepsilon) = \sqrt{\frac{\varepsilon(1-\varepsilon)}{N}} \ .$$

The charged lepton originating from a right-handed W-boson is emitted into the flight direction of the W, whereas the left-handed W emits the charged lepton opposite to its flight direction. This results in a harder lepton p_T-spectrum for the right-handed case. The distribution for the left-handed case peaks at lower values. After applying a cut of $p_T > 20$ GeV/c, right handed events are more likely to pass the event selection, compared to the relative efficiencies in Tab.4.2 and 4.3. This implies that the efficiency of the event selection for left-handed W-bosons is smaller than for the longitudinal and right-handed W-boson. The efficiency of the right-handed template is expected to be the largest. Although the longitudinal template has the largest absolute efficiency, the right-handed template has the largest efficiency due to the cut on the transverse momentum.

Criterion	SM sample	ε_{rel}	ε_{abs}	F_0 sample	ε_{rel}	ε_{abs}
Total no. events	98,966			99,987		
pre-selection	77,695	1.000	1.000	78,451	1.000	1.000
1	22,687	0.292	0.292	24,646	0.314	0.314
2	20,380	0.898	0.262	21,883	0.888	0.279
3	12,312	0.604	0.158	13,453	0.615	0.171
4	10,771	0.875	0.139	11,763	0.874	0.150
$p_T < 200$ GeV/c	10,652	0.989	0.137	11,621	0.988	0.148

Table 4.2: Cut Flow for the event selection of the SM data set and the F_0 template. ε_{rel} is the relative efficiency of the selected events compared to previous cut. ε_{abs} is the total efficiency of the selected events compared to the amount of pre-selected events. The numbers 1-4 indicate the selection criteria in Chapter 4.4.1.

One gets a total efficiency for each sample of:

$$\begin{aligned} \varepsilon_{SM} &= 0.137 \pm 0.001 \\ \varepsilon_{F_0} &= 0.148 \pm 0.001 \\ \varepsilon_{F_-} &= 0.115 \pm 0.001 \\ \varepsilon_{F_+} &= 0.143 \pm 0.001 \ . \end{aligned}$$

Criterion	F_- sample	ε_{rel}	ε_{abs}	F_+ sample	ε_{rel}	ε_{abs}
Total no. events	100000			95000		
pre-selection	78,689	1.000	1.000	74,656	1.000	1.000
1	19,329	0.246	0.246	25,532	0.342	0.342
2	18,016	0.932	0.223	21,061	0.825	0.282
3	10,578	0.587	0.134	12,552	0.596	0.168
4	9,114	0.862	0.116	11,004	0.877	0.147
$p_T < 200$ GeV/c	9,085	0.997	0.115	10,676	0.970	0.143

Table 4.3: Cut Flow for the event selection of the F_- and F_+ template. ε_{rel} is the relative efficiency of the selected events compared to previous cut. ε_{abs} is the total efficiency of the selected events compared to the amount of pre-selected events. The numbers 1-4 indicate the selection criteria in Chapter 4.4.1.

5 Statistical Tools

In this chapter the statistical tools for the analysis are presented. The reconstruction of the $t\bar{t}$ events is based on the Maximum Likelihood Method which is implemented in the KLFitter. The helicity fractions of the W-boson are determined by applying the Template Method.

5.1 Maximum Likelihood Method

The distribution of a variable x is described by the probability density function $f(x;\theta_1,...,\theta_k)$. The variable x could also be a multidimensional vector. The maximum likelihood method estimates the values of the parameters $\theta_1,...,\theta_k$ given a sample of data using the likelihood function. The variable x is measured n times in independent measurements resulting in the data sample $\{x_1,...,x_n\}$. The Likelihood function is defined as:

$$L(\theta_1,...,\theta_k) = \prod_{i=1}^{n} f(x_i;\theta_1,...,\theta_k) \ .$$

The best estimation of the parameters $\theta_1,...,\theta_k$ are the values for which the Likehood function is maximized:

$$\frac{\partial L}{\partial \theta_i}|_{\theta_i=\hat{\theta}_i} = 0 \quad i = 1,...,k \ .$$

Because of the monotony of the logarithm it is often more convenient to maximize the Log-Likelihood function:

$$l = \log L(\theta_1,...,\theta_k) = \sum_{i=1}^{n} \log f(x_i;\theta_1,...,\theta_k)$$

or to minimize $-\log L$.

5.2 KLFitter

In leading order the semileptonic $t\bar{t}$ decay channel comprises two light quarks from the hadronically decaying W-boson, two b-quarks, one charged lepton and its corresponding neutrino. Therefore 24 permutations are possible to associate the jets with the quarks. Taking into account that the quarks of the hadronically decaying W-boson cannot be distinguished, still 12 permutations remain. To reconstruct the $t\bar{t}$ events and find the best jet-parton mapping, the *Kinematic Likelihood Fitter* (KLFitter) is used which is based on a Likelihood approach [34].
For the reconstruction of a $t\bar{t}$ event the energies and angles of the four jets (E_{i}, Ω_{i}), of the charged lepton (E_{l}, Ω_{l}) and the missing transverse energy of the neutrino (E_{T}^{miss}) are used from the measurements. The uncertainties due to the measurement are parametrised by the transfer functions W. $\mathrm{W}(E_{\mathrm{true}}|E_{\mathrm{meas}})$ describes the probability that the measured energy of a particle is E_{meas} if the true energy of the particle is E_{true}. These transfer functions are parametrised by a double Gaussian function. The transfer functions used in the KLFitter have been extracted from semileptonic $t\bar{t}$ - samples which have been generated with MC@NLO and passed through the full ATLAS reconstruction. The angles (η_l, ϕ_l) of the charged lepton are assumed to be measured precisely. Futhermore it has to be taken into account that the invariant mass of the two light jets and the invariant mass of the lepton and the corresponding neutrino are Breit-Wigner distributed around the W pole mass $BW(m_{jj}, m_W), BW(m_{e\nu}, m_W)$. Moreover the invariant mass of the b-jet and the two light jets is Breit-Wigner distributed around the top-quark pole mass and analog for the invariant mass of the b-jet, the charged lepton and the neutrino $BW(m_{jjj}, m_t), BW(m_{e\nu j}, m_t)$. The pole mass of the top quark can either be fixed or be a free parameter.
The likelihood function is:

$$\begin{aligned} L = \left(\prod_{i=1}^{4} W(\widetilde{E}_i, E_i)\right) \quad &\cdot \quad W(\widetilde{E}_l, E_l) \cdot W(E_x^{miss}, p_x^{\nu}) \cdot W(E_y^{miss}, p_y^{\nu}) \cdot \\ \left(\prod_{i=1}^{4} W(\widetilde{\Omega}_i, \Omega_i)\right) \quad &\cdot \quad BW(m_{jjj}, m_t) \cdot BW(m_{e\nu j}, m_t) \cdot BW(m_{jj}, m_W) \cdot BW(m_{e\nu}, m_W). \end{aligned} \tag{5.1}$$

To determine the maximum of the Likelihood function, the minimum of -ln L is calculated for each possible combination. The combination with the highest likelihood value defines the best jet-parton mapping and is used for the event reconstruction.

The KLFitter is based on the BAT - package [35] which provides integration methods and phase-space sampling using either Markov Chain Monte Carlo or Minuit.

5.3 The Template Method

The helicity fractions of a given data set are determined by applying the template method. This method uses the three templates for the different helicity states and fits their relative contribution to the data. The aim of the fit is to determine the number of longitudinal, left- and right-handed W-boson events before applying any cuts. Each helicity fraction $\mathrm{F_j}$, $j = 0, +, -$ contributes with $\mathrm{N_j}$ events, which are Poissonian distributed around the expectation value $\lambda_\mathrm{j}^\mathrm{exp}$ to the data set. The expected value λ_i for each bin i is then:

$$\lambda_\mathrm{i} = \sum_{j=0,+,-} \lambda_\mathrm{j}^\mathrm{exp} \int_{\Delta x_\mathrm{i}} f_\mathrm{j}(x)\mathrm{d}x,$$

where Δx_i is the bin width and f_j the probability density which is parametrised by the templates for the helicity fractions. For the fit no prior probabilities are used. In order to get the number of events $\mathrm{N_j}$ before applying cuts, the absolute efficiencies, calculated in Chapter 4.4.2 have to be taken into account via

$$\lambda_\mathrm{i} = \sum_{j=0,+,-} \varepsilon_{abs} \cdot \lambda_\mathrm{j}^\mathrm{exp} \int_{\Delta x_\mathrm{i}} f_\mathrm{j}(x)\mathrm{d}x \ .$$

The best fit values are those which maximize the Likelihood function. The Likelihood function is the product of Poissonian distributions :

$$p(n_\mathrm{data}, \lambda_\mathrm{i}) = \prod_i^{N_\mathrm{bins}} \frac{\lambda_\mathrm{i}^{n_\mathrm{i}}}{n_\mathrm{i}!} \cdot e^{-\lambda_\mathrm{i}},$$

where n_i is the number of events in bin i and λ_i the expectation values for the fit parameters. The maximization of the Likelihood function can be found with Minuit or with Markov Chains which are implemented in the BAT package.

Ensemble Testing

Due to the limited number of events in one data set, ensemble tests are performed. A number of 5,000 ensembles is created with each 3825 events. To create an ensemble,

each bin entry of the data set is fluctuated according to a Poissonian distribution. Therefore the total number of events in one ensemble is not fixed to a certain value. Afterwards the templates are fitted to the 5,000 ensembles and the fit results and their errors are histogrammed. Ensemble tests are also used to study the statistical uncertainties.

6 Results

In this chapter the result of the analysis using the transverse momentum of the charged lepton are summarised. After a first application of the Template Method, the statistical uncertainties and systematical uncertainties are evaluated. Moreover the correlation between the spin analyser cos θ^* and p_T is calculated.

6.1 Templates

The Standard Model data set and the three templates are depicted in Fig.6.1 on generator level (dots) and after the detector simulation (cross). Poissonian errors are drawn in each bin.

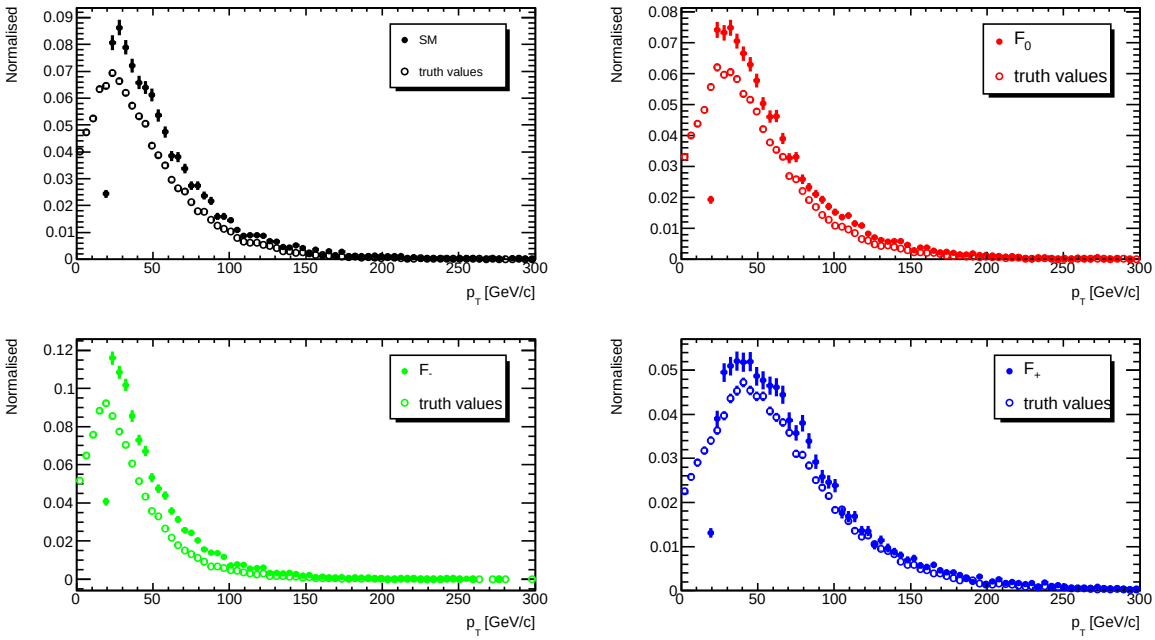

Figure 6.1: Comparison between the p_T-distributions on generator level (circle) and after the the detector simulation (dots). The distributions are normalised to unity.

Fig. 6.2 shows the distributions of the SM and the three helicity states on generator level.

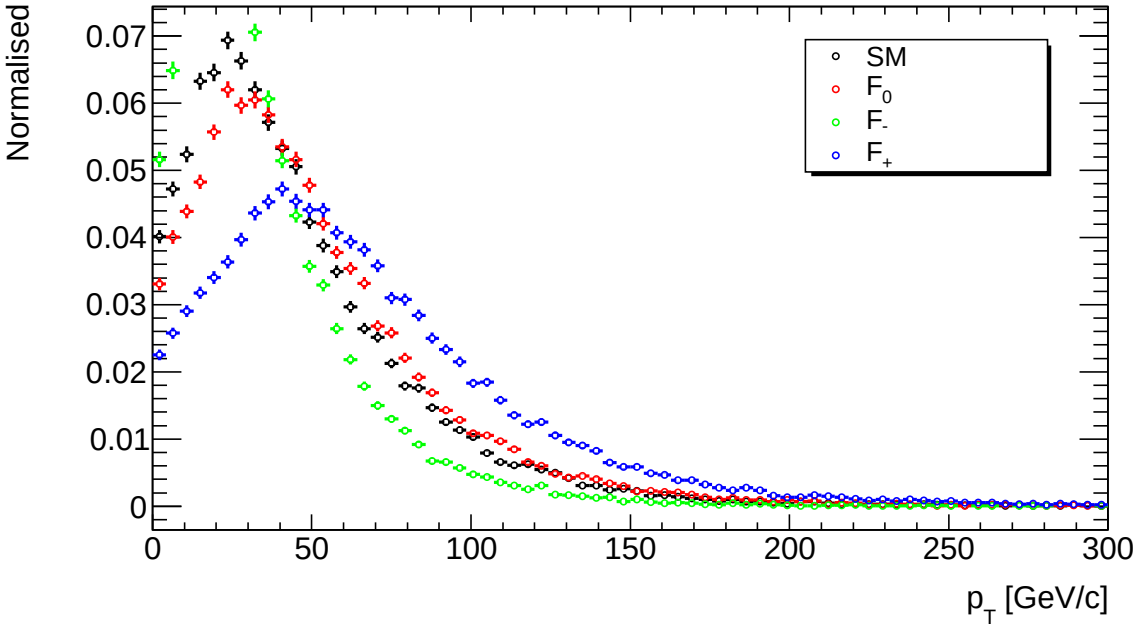

Figure 6.2: Comparison between the p_T-distributions for the SM dataset and the three helicity templates on generator level. The distributions are normalised to unity.

The distributions for the left-handed and the right-handed case show a different behaviour. The right-handed distribution is much broader and peaks at higher values. Nevertheless, the distributions are much more similar than the ones shown for $\cos\theta^*$ (see Chapter 2.3.1).

6.2 First Fit

The Template Method was first applied to a data set which has been generated using the three templates according to the Standard Model expectation: $F_0 = 0.7$, $F_- = 0.3$, $F_+ = 0.0$. The data set is scaled to $\mathcal{L} = 200$ pb^{-1} and a center-of-mass energy of $\sqrt{s}$ =10 TeV via

$$N_{\text{exp}} = \varepsilon \cdot \sigma \cdot \mathcal{L} \cdot BR, \tag{6.1}$$

where σ is the cross-section, N_{exp} the expected number of events and BR the branching ratio. The cross-section for the production of $t\bar{t}$ events at $\sqrt{s} = 10$ TeV is $\sigma_{t\bar{t}} = 401.6$ pb $\pm^{3.6\%}_{4.3\%} \pm^{4.6\%}_{4.5\%}$ [7]. The semileptonic decay channel with one electron has a cross-section of $\sigma_{t\bar{t}\to e+jets} = 69.28$ pb.
According to the efficiencies in Tab. 4.2, the expected number of events is:

$$N_{\text{exp}} = 3825 \ ,$$

assuming a Branching Ratio of 0.1725 for the e + jets and μ + jets channel equally.

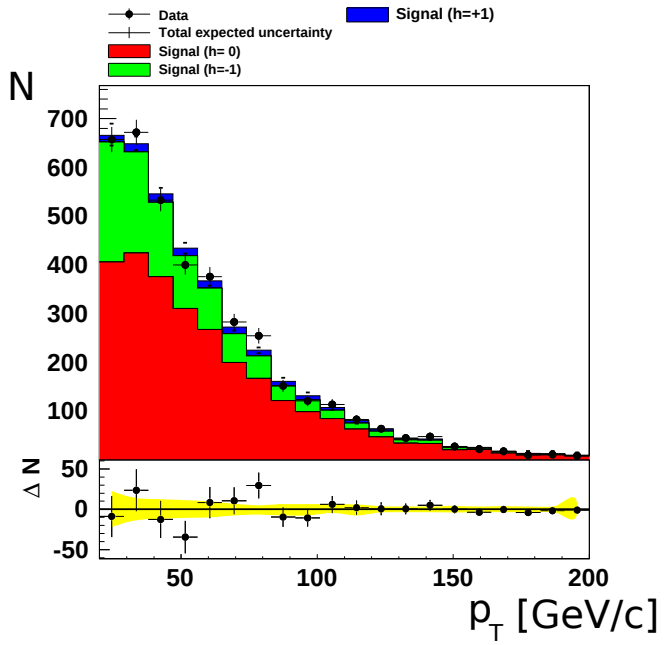

Figure 6.3: Template Fit of a Standard Model data set. The residual distribution shows the level of agreement between the fit results (histogram) and the data (black points). The χ^2 per number of degrees of freedom is 0.548562.

Fig. 6.3 shows the template fit of the composed Standard Model data set. The fit values for the helicity fractions are:

$$\begin{aligned} F_0 &= 0.63 \pm^{0.23}_{0.22} \ , \\ F_- &= 0.32 \pm^{0.12}_{0.13} \ , \\ F_+ &= -0.044 \pm^{0.11}_{0.11} \ . \end{aligned}$$

The estimated values of the fit are consistent with the input values.
Furthermore, an ensemble test has been performed using 5,000 ensembles. The procedure has been explained in chapter 5.3. Minuit has been used to perform the fits. The left plot in Fig.6.4 shows the distribution of the mode for the estimated number of longitudinal events. The expected number of longitudinal events before the selection cuts for the Standard Model data sets is 19388. The mean value of the mode is 19470 $\pm$ 81.15 and is consistent within the errors. As it can be seen, the statistical uncertainties of the different helicity states are symmetric Gaussian distributed. The statistical errors are symmetric.

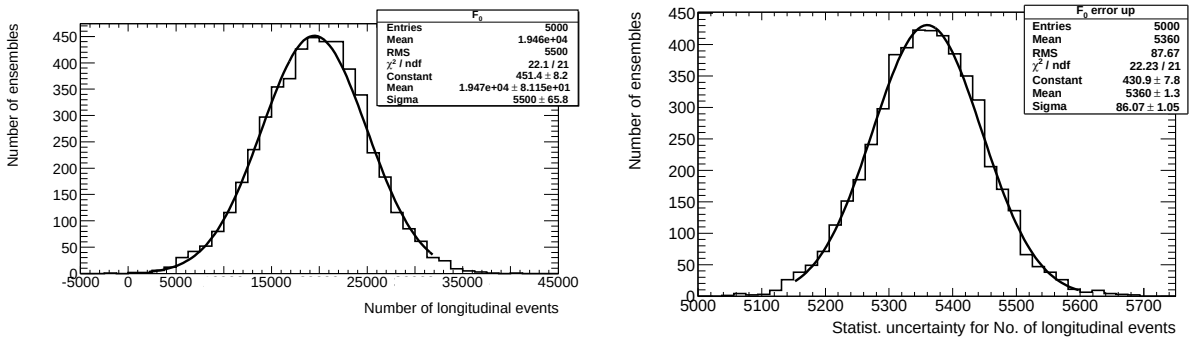

Figure 6.4: Left plot: Distribution of the mode for the fitted number of longitudinal events. The right distribution shows the statistical uncertainties of the estimated mode.

6.2.1 Pull-distribution

In order to check the agreement of the fit result with the input values, the pull distribution is used:

$$p_i = \frac{y_i - y_{\text{exp}}}{\sigma_i} \ ,$$

where y_i is the measured value, y_{exp} the expected value from the model and σ_i the error of the data. The pull distribution is expected to be a Gaussian with a mean value of $\mu = 0$ and a standard deviation of $\sigma = 1$. Fig. 6.5 shows the pull distributions of the different helicity states for the data set with expected fractions of the Standard Model.
The mean value of the pull distribution for the left-handed events is consistent with the expected value. The mean of the right-handed pull is very close to zero and consistent within the error range of 2 sigma.

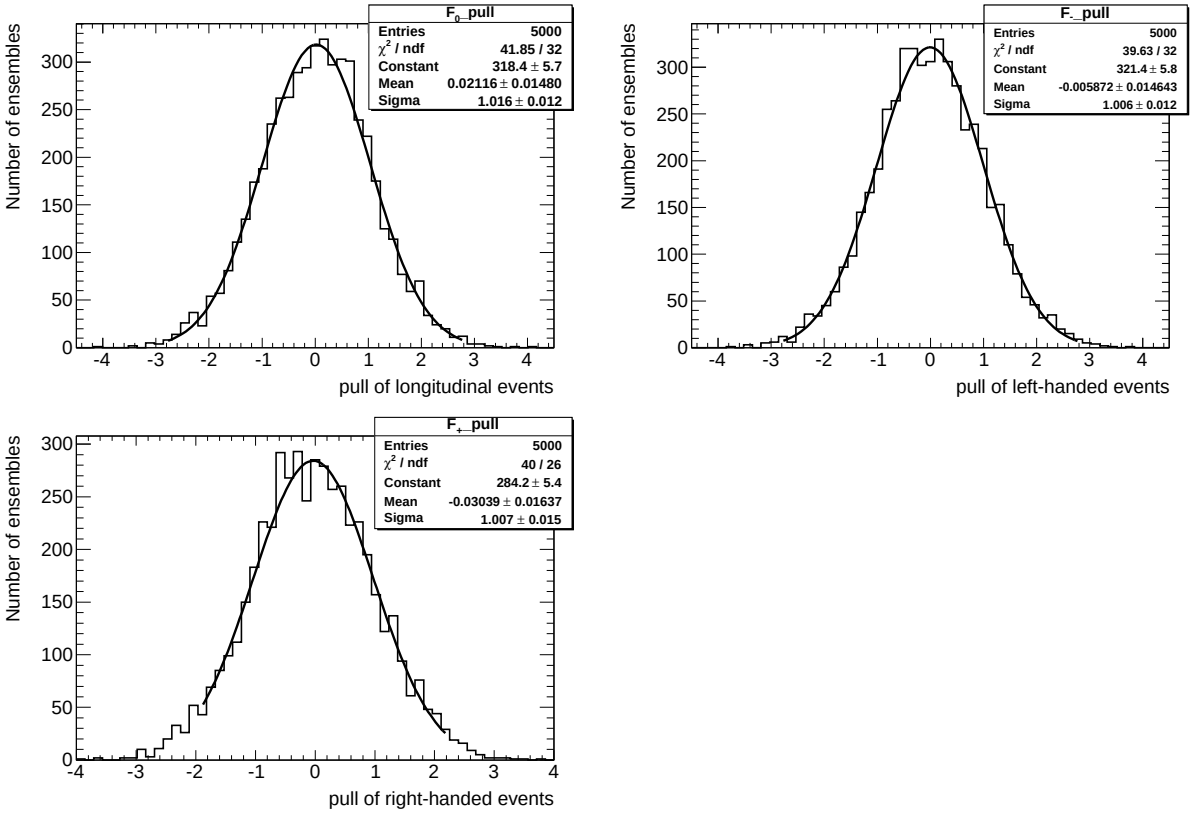

Figure 6.5: Pull distributions of the different helicity states for the data sample with $F_0 = 0.7$ and $F_- = 0.3$. On the upper left side the distribution for F_0 is shown. The upper right and lower left side shows the results for F_- and F_+ respectively.

6.3 Calibration Curves

The ensemble test analysis has been applied to seven Monte Carlo data sets with different helicity compositions. The first data set comprises the helicity fractions according to the Standard Model $F_0 = 0.7$, $F_- = 0.3$, $F_+ = 0.0$. The other data sets are generated by increasing the right-handed helicity fractions in steps of 0.025 and simultaneously uniformly decreasing the longitudinal and left-handed fractions. All data sets contain only signal events and are scaled to $\mathcal{L} = 200\ \mathrm{pb}^{-1}$. Furthermore negative parameters are allowed in the fit procedure. Fig. 6.6 shows the estimated helicity fractions from the fit for 5000 ensembles as a function of the input fractions. The graphs are fitted with a linear function. The linear functions are supposed to have a slope of one and an offset of zero. Furthermore the development of the χ^2 as a function of the right-handed fraction is depicted.

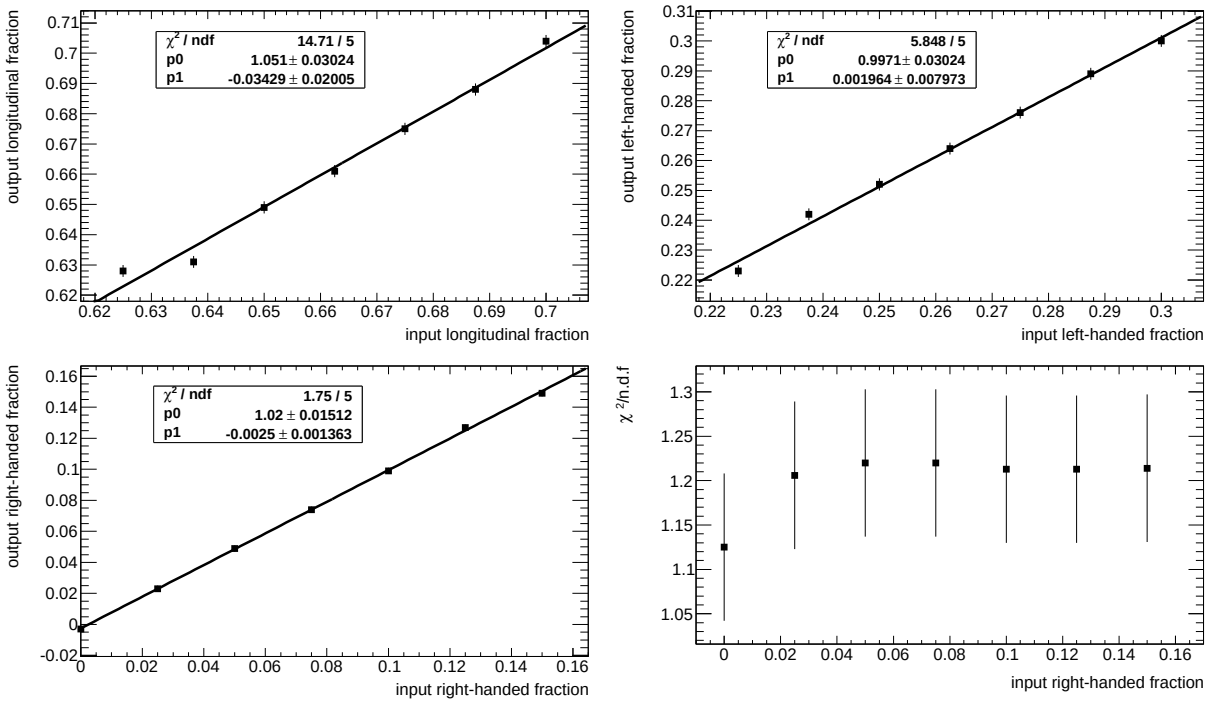

Figure 6.6: Calibration curves for only signal events for the longitudinal, left-handed and right-handed helicity fractions. For the right-handed fractions the errors are too small to be seen. The bottom right plot shows the χ^2 per number of degrees of freedom as a function of the right-handed fraction.

The estimated slope and offset of the left-handed fractions is consistent with the expected slope within the errors. The slope and offset of the longitudinal and right-handed fractions are in the 2σ region.

6.3.1 Calibration Curve with Physical Limits

The seven generated Monte Carlo data sets which are described above are also fitted by admitting only positive parameters in the fit. Therefore, the distributions of the longitudinal, left-handed and right-handed events are biased. Again 5000 ensembles were produced. Fig. 6.7 shows the estimated helicity fractions from the fit as a function of the input fractions.

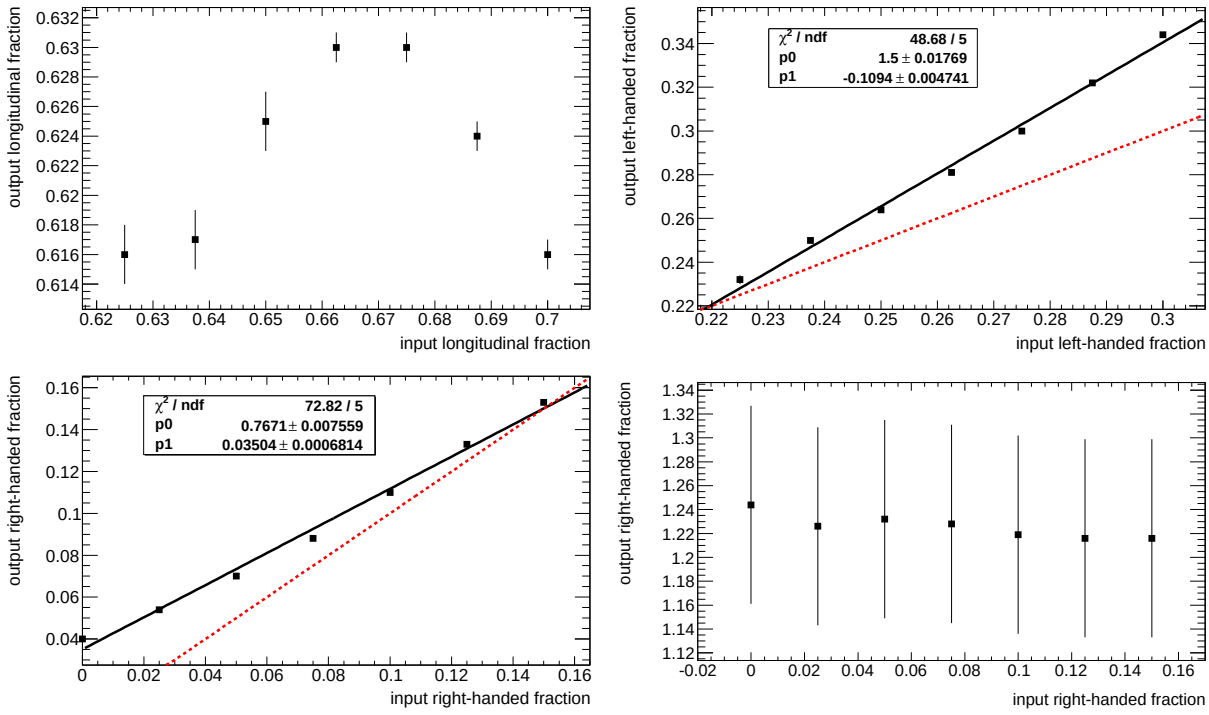

Figure 6.7: Calibration Curve with physical limits for the three helicity states. The dotted line implies the expected curve.

The dotted line represents the expected linear behaviour between input and output fractions. For small right-handed fractions one expects a significant difference between the expected curve and the fitted curve due to the bias. This behaviour is observed in the lower left plot of Fig. 6.7.

6.3.2 Calibration Curve with Background

Tab. 6.1 contains the expected number of events for the different background contributions of semileptonic $t\bar{t}$ decays in electron + jets. The left column comprehends the events after the pre-selection cut and the cuts 1-4, see Chapter 4.1.1. If one

considers only transverse momenta with $p_T < 200$ GeV/c, the numbers in the right columns are estimated. All events are again scaled to $\mathcal{L} = 200$ pb^{-1}. Furthermore the signal to background ratio is indicated.

	e + jets		e+jets, $p_T < 200$ GeV/c	
Signal	nr. events	Uncertainty	nr. events	Uncertainty
	3859	21	3825	21
Background	nr. events	Uncertainty	nr. events	Uncertainty
$t\bar{t}$ dilepton	443	12	436	12
$t\bar{t}$ hadronic	39	2	38	2
single top	308	9	304	9
diboson	23	1	22	1
Wbb + jets	46	2	44	2
Z(ee) + jets	138	5	131	5
Z($\mu\mu$) + jets	0	0	0	0
Z($\tau\tau$) + jets	69	2	68	2
W(eν) + jets	2122	22	2058	22
W($\mu\nu$) + jets	5	1	5	1
W($\tau\nu$) + jets	182	7	179	7
Total Background	3375	28	3285	28
S/B	1.16		1.16	
$S/\sqrt{S+B}$	45.48		45.36	

Table 6.1: Number of background events for the e+jets channel in $t\bar{t}$ decays before (left columns) and after (right columns) the critera $p_T < 200$ GeV/c.

The background contributions were added respectively to the seven created signal samples. For each sample 5000 ensembles were fitted. Fig. 6.8 depicts the three different helicity fractions of the fit plotted versus the input fractions. The slope of the linear function is supposed to be unity. The parameters for the slope of the fitted functions are consistent for the left- and right-handed fraction. The slope for the longitudinal is in the 2σ region.

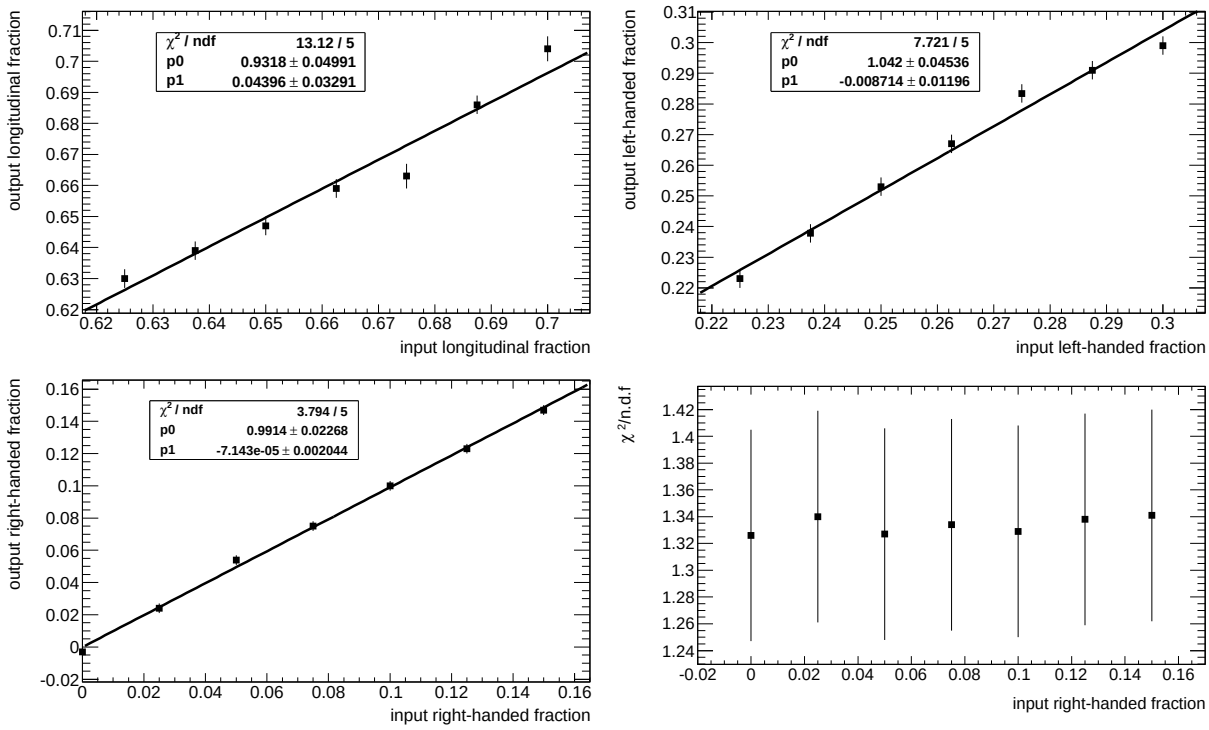

Figure 6.8: Calibration curves for the longitudinal, left-handed and right-handed helicity fractions with background contribution. The fit parameters are allowed to be negative.

6.4 Statistical Uncertainties

The statistical uncertainties of the three helicity states as obtained from the ensemble tests for the created Standard Model data set are shown in Fig. 6.9.
The relative errors compared to the total expected number of events in the signal samples are quoted in Tab. 6.2. Furthermore, the relative errors for a data set with background contributions are noted. The errors from a fit with background contribution are obviously larger.

	error (long. events)	error (left-h. events)	error (right-h. events)
signal	0.194	0.126	0.105
signal+bkg	0.270	0.250	0.175

Table 6.2: Relative errors for the nr. of longitudinal, left- and right-handed events for the spin analyser p_T for a pure signal sample (up) and a data sample with background contribution (bottom).

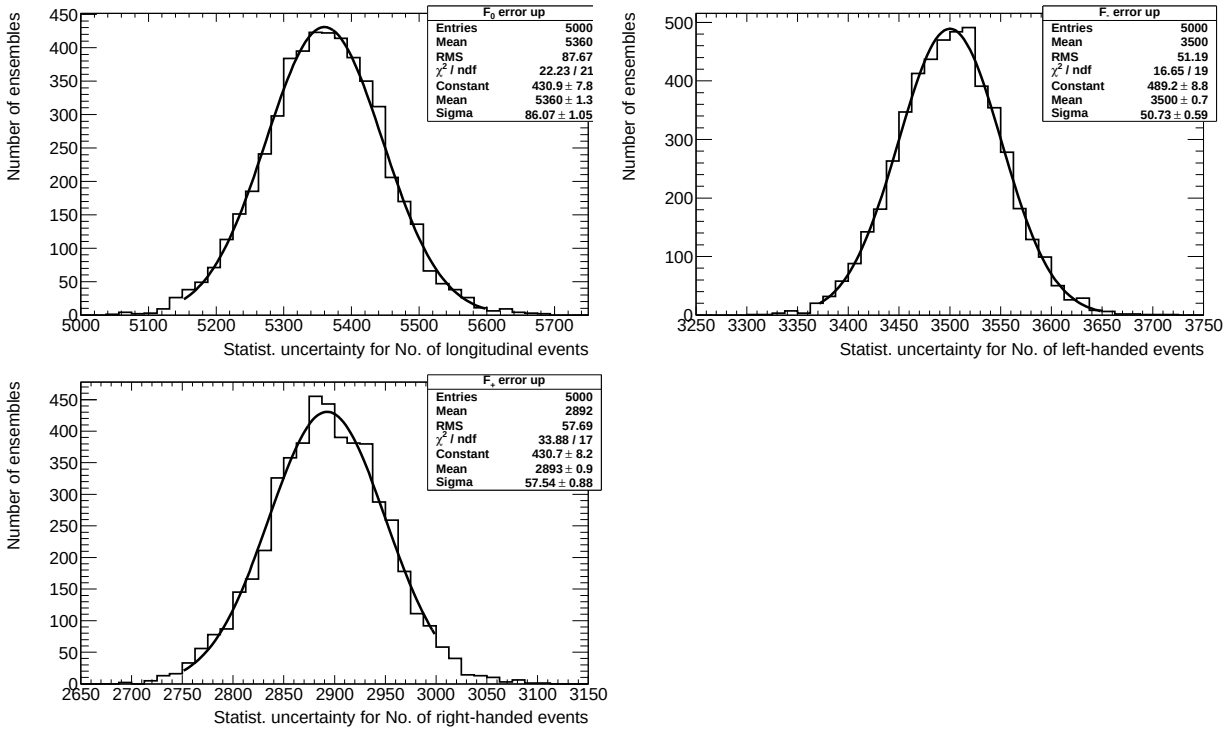

Figure 6.9: Statistical uncertainty distributions for the longitudinal (upper left), left-handed (upper right) and right-handed (below) number of events in the Standard Model data set.

6.5 Systematic Uncertainties

Due to the large number of $t\bar{t}$-events expected at the LHC after two years of running, the measurements of the helicity fractions will be limited mainly by systematic uncertainties. Studies of these uncertainties are presented in the following chapter. The samples used for these have different integrated luminosity. Therefore ensembles with and with background contribution were produced by taking N_{exp} random numbers out of these samples, where N_{exp} is the expected amount of events for an integrated luminosity of $\mathcal{L} = 200$ pb^{-1}. The expected number of events in a pure signal sample is 3825 wheres the number of background events is expected to be 3285. The helicity fractions are calculated using the mode and the corresponding error of the histogrammed fit values.

6.5.1 Top Quark Mass

The W-helicity fractions depend directly on the top quark mass as explained in Chapter 2.3. The samples used to create the templates are generated with 172.5

GeV/c^2. In order to estimate the uncertainty due to the mass of the top quark, three signal samples are used with different top masses of m_t=160, 170, 180 GeV/c^2. 3000 ensemble tests have been performed. The top quark mass has been used as a free parameter in the fit. The fractions of the helicity states are plotted against the top mass, see Fig. 6.10 and fitted with a linear function. The spin analyser $\cos\theta^*$ depends linearly on the top quark mass. In order to be comparable the linear correlation has been chosen. Nevertheless the behaviour could also be nonlinear as indicated in Chapter 2.3. The systematic uncertainty is given as the variation of a top mass change of $\pm$ 2.5 GeV/c^2 which is twice the uncertainty of the current world average mass.

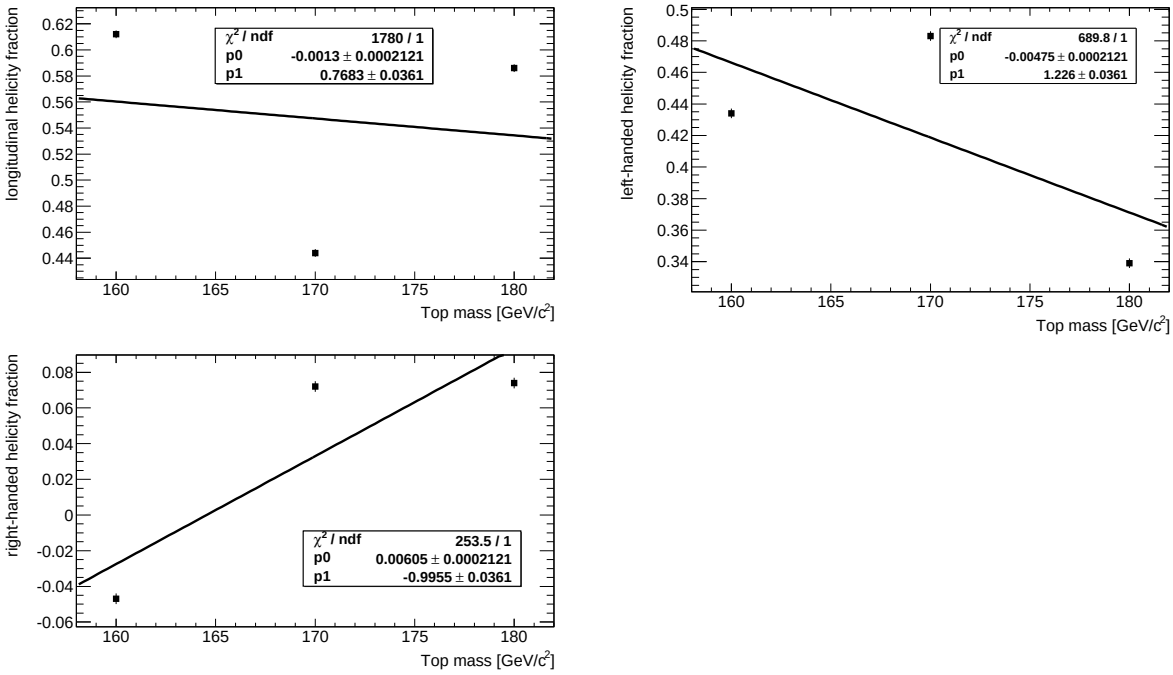

Figure 6.10: Dependence of the helicity fractions of the top quark mass. The upper left plot shows the distribution for the longitudinal fractions, the upper right plot for the left-handed and the plot below for the right-handed fraction.

As shown in Fig. 6.11, the left- and right-handed fraction are highly correlated whereas their correlation coefficient with the longitudinal fraction is negative. The fits for the top mass uncertainty show that the right-handed fraction is overestimated. Being that much correlated to the left-handed fraction, this one is also overestimated. This leads in a very significant underestimation of the longitudinal fraction. For this reason, the evaluation of the uncertainties is also repeated with a

fixed right-handed fraction. The results are shown in Fig. 6.12 and are compared in Tab. 6.3.

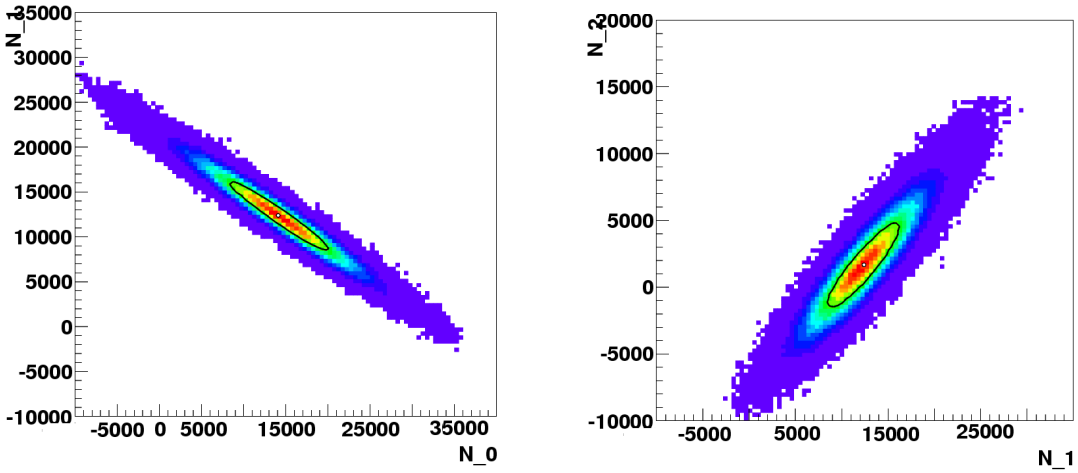

Figure 6.11: Correlation between the longitudinal (N_0) and left-handed events (N_1) (left plot) and the left- handed (N_1) and right handed fraction (N_2) (right plot).

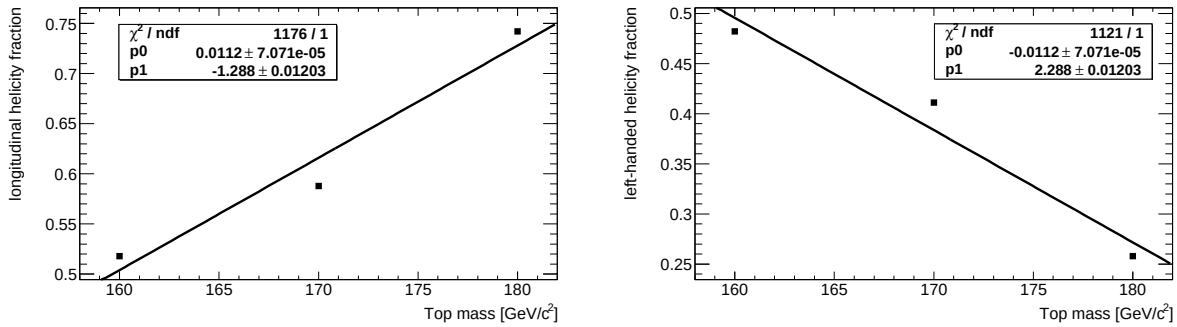

Figure 6.12: Dependence of the helicity fractions of the top quark mass with a fixed right-handed fraction.

	F_+ included	F_+ fixed
F_0	0.003	0.028
F_-	0.012	0.028
F_+	0.015	-

Table 6.3: Systematic Uncertainties due the top mass for the three helicity states without and with a fixed right-handed fraction

6.5.2 Lepton Energy Scale

The *Lepton Energy Scale* (LES) describes the under- or overestimation of the lepton energy in the electromagnetic calorimeter. The energies of the leptons could e.g. be underestimated if energy is deposited in dead material. The energy of the lepton is changed by ± 1%. In this analysis, the impact of the LES is investigated by varying the templates instead of the pseudodata. For each lepton energy scale, templates for the three helicity fractions are produced. The event selection and reconstruction procedures are applied as before. The templates corresponding to the three different LES are fitted to 3000 ensembles of a Standard Model data set. Fig. 6.13 shows the the estimated helicity fractions depending on the used LES. The values are fitted with a straight line and the slope estimates the systematic uncertainty. A straight line is expected because the templates have been varied instead of the SM data set by fluctuating the lepton momenta by ± 1%.

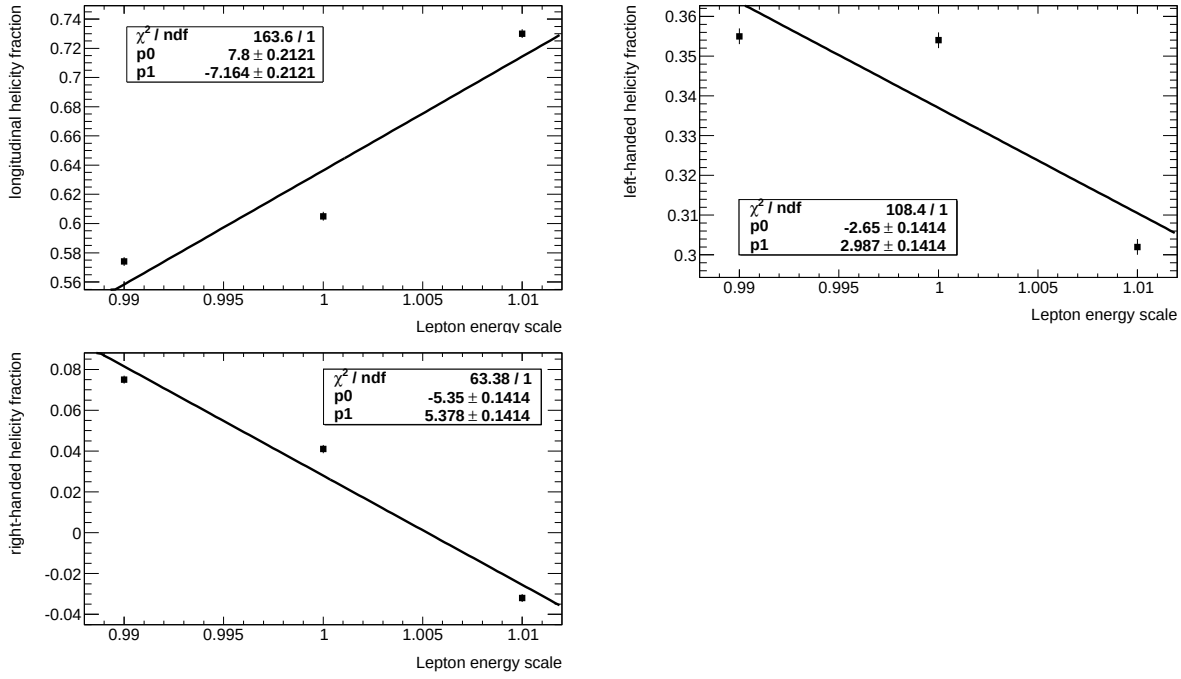

Figure 6.13: Estimation of the Lepton Energy Scale for the scaled momentum of ± 1 % and the nominal sample. The value 1.01 indicates the scaled LES of 1 %.

Fig. 6.14 contains the longitudinal and left-handed fraction depending on the LES for a fixed right-handed fraction.

The comparison between the systematic uncertainties for the fits with three tem-

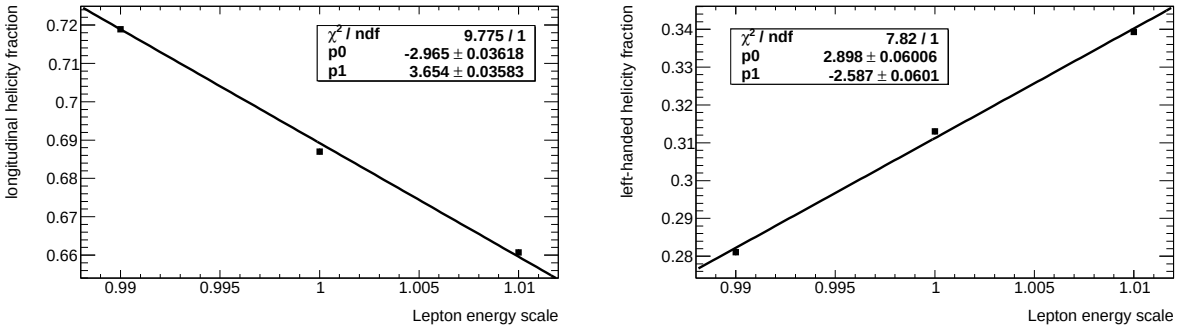

Figure 6.14: Estimation of the Lepton Energy Scale systematic uncertainty for the scaled momentum of ± 1% and the nominal sample with a fixed right-handed fraction. The errors are to small to be seen.

plates and for the fits with a fixed right-handed fraction is shown in Tab. 6.4. As it

	F_+ included	F_+ fixed
F_0	0.078	0.030
F_-	0.027	0.029
F_+	0.054	-

Table 6.4: Systematic Uncertainties for the lepton energy scale for the three helicity states without and with a fixed right-handed helicity.

can be seen, the systematic uncertainty for the longitudinal fraction is smaller for a two dimensional fit than for the three dimensional fit as expected. The growth of the uncertainty for the left-handed fraction is very small and could be explained by statistical fluctuations.

6.5.3 Jet Energy Scale

At the LHC and hadron colliders in general the largest source of systematic errors is the *jet energy scale* (JES). Due to initial and final state radiation or out-of-cone showering the energy can be measured too low. This can also happen if particles deposit a part of their energy in dead detector material. Overlapping jets for example would lead to an overestimated jet energy.

The influence of the JES is investigated by scaling the four-momentum of the reconstructed jets in the hadronic calorimeter by 5%. Analogue to the LES, the two new template sets are passed through the full chain of event selection and reconstruction and are then fitted to 3000 Standard Model ensembles.

The output fractions are plotted as a function of the JES variation, using a three (see

Fig. 6.15) or a two parameter fit (Fig. 6.16). Analogue to the LES we expect a linear dependence. The slope of the linear function indicates the systematic uncertainty for a JES variation of 5%. For the spin analyser p_T one expects only a negligible

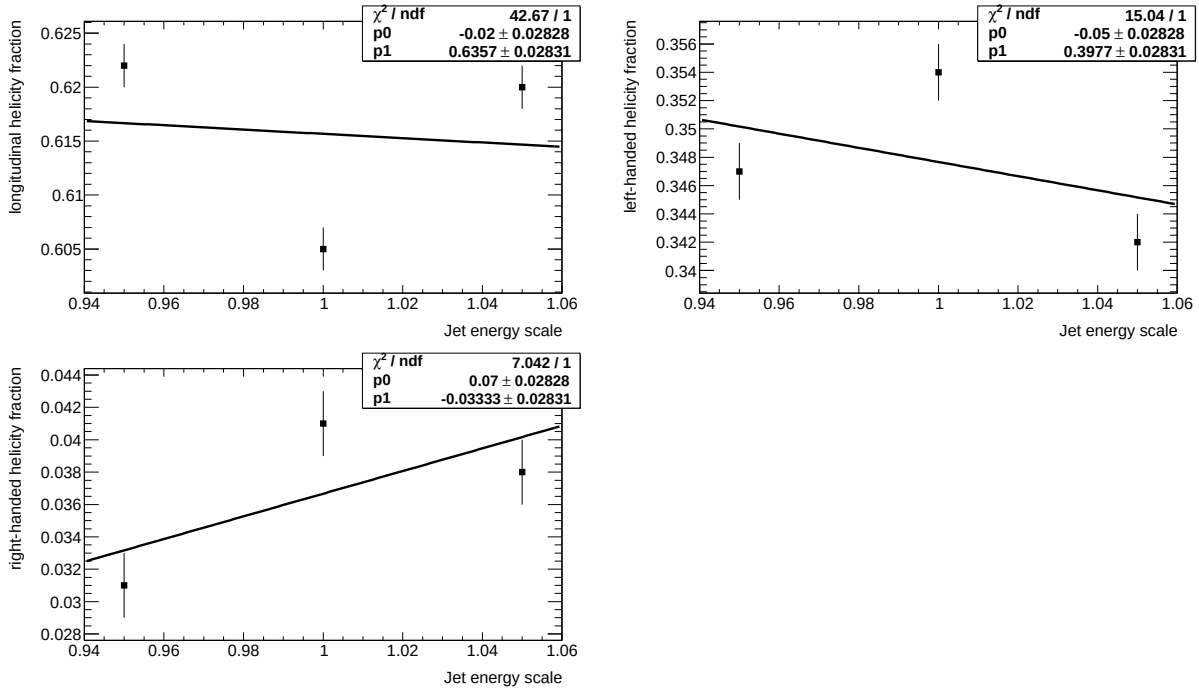

Figure 6.15: Helicity fractions as a function of the jet energy scale.

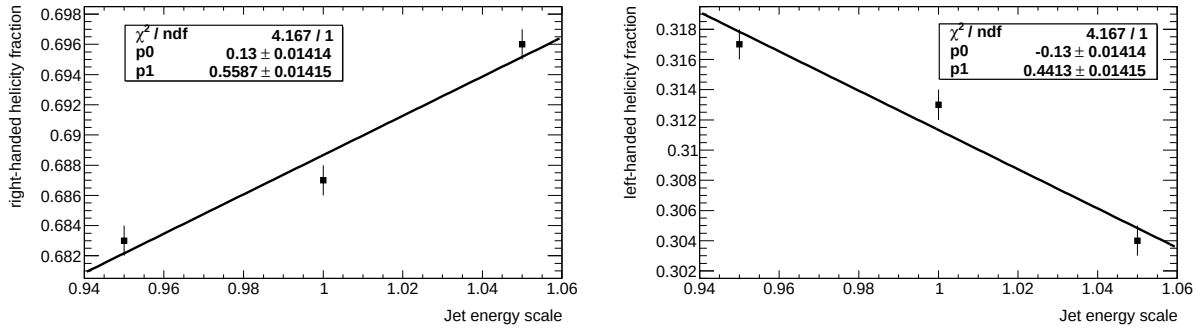

Figure 6.16: Helicity fractions as a function of the jet energy scale with a fixed right-handed fraction. The value 1.05 indicates the scaled JES of 5 %.

influence on the JES. This can be seen in Tab. 6.5 which summarises the uncertainties for the three helicity states. As it can be seen in Tab. 6.5 the uncertainty for a fixed right-handed fraction is bigger than the uncertainties for the three dimensional fit. This behaviour has not been expected and needs further investigations.

syst. uncertainty	F_+ included	F_+ fixed
F_0	0.001	0.007
F_-	0.003	0.007
F_+	0.004	-

Table 6.5: Systematic Uncertainties for the jet energy scale for the three helicity states without and with a fixed right-handed fraction.

6.5.4 Initial and Final State Radiation

Initial and final state radiation (ISR and FSR) have an effect on the transverse spectrum and on the features of the jets. Three different samples are generated with AcerMC which have different cutoff parameters: one sample with ISR, one sample with FSR and the nominal sample without radiation. For each sample 3000 ensembles were fitted. Tab. 6.6 shows the estimated helicity fractions for the nominal sample and for the samples which include intial and final state radiation. Furthermore the difference of the fractions from the ISR and FSR samples with respect to the nominal one is illustrated.

	nominal sample	ISR sample	FSR sample	variation ISR	variation FSR
F_0	0.386 ± 0.003	0.478 ± 0.003	0.382 ± 0.002	0.092	0.004
F_-	0.461 ± 0.003	0.403 ± 0.003	0.468 ± 0.003	0.062	0.007
F_+	0.153 ± 0.002	0.119 ± 0.002	0.150 ± 0.002	0.034	0.003

Table 6.6: Helicity fractions for the nominal sample and the samples with initial state radiation (ISR) and final state radiation (FSR) respectively. The variation describes the difference between the nominal sample and the ISR and FSR respectively.

The largest variation for each helicity state is an estimator for the systematic uncertainty. This study has been repeated with a fixed right-handed fraction.

	nominal sample	ISR	FSR	variation ISR	variation FSR
F_0	0.692 ± 0.001	0.717 ± 0.001	0.684 ± 0.001	0.025	0.008
F_-	0.308 ± 0.001	0.283 ± 0.001	0.316 ± 0.001	0.020	0.033

Table 6.7: Helicity fractions for the nominal sample and the two samples with initial state radiation (ISR) and final state radiation (FSR) with a fixed right-handed fraction. The variation describes the difference between the nominal sample and the ISR and FSR respectively.

As expected, the systematic errors are smaller for a fit with only longitudinal and

left-handed helicity templates, as it can be seen in 6.7. The right-handed fraction is fixed to its Standard Modell prediction, therefore the helicity fractions can be determined in a two dimensional fit which reduces the uncertainties.

	F_+ included	F_+ fixed
F_0	0.092	0.025
F_-	0.062	0.033
F_+	0.034	-

Table 6.8: Summary of the systematic uncertainites due to initial and final state radiation for an included right-handed fraction and a fixed right-handed fraction.

6.5.5 Monte Carlo Generators

The systematic uncertainties due to the MC generators are estimated by comparing the fit results for the AcerMC (LO) and the MC@NLO (NLO) generators. For each generator a 3000 sample has been produced and were fitted with the templates with pure helicity fractions. The parameters of the fit for the two generators are noted in Tab. 6.9 and Tab. 6.10. The systematic uncertainties are taken as the difference of the two generators.

	AcerMC	MC@NLO	variation
F_0	0.386 ± 0.003	0.603 ± 0.003	0.223
F_-	0.461 ± 0.003	0.392 ± 0.003	0.069
F_+	0.153 ± 0.002	0.005 ± 0.003	0.148

Table 6.9: Helicity fractions for the AcerMC and MC@NLO Monte Carlo generator.

	AcerMC	MC@NLO	variation
F_0	0.692 ± 0.001	0.613 ± 0.001	0.079
F_-	0.308 ± 0.001	0.387 ± 0.001	0.079

Table 6.10: Helicity fractions for the AcerMC and MC@NLO Monte Carlo generator with a fixed right-handed fraction.

6.5.6 Hadronisation

The hadronisation of the jets in the generated samples are either described by a string model or by a cluster model. Two samples are generated with AcerMc using

the showering of Pythia (string model) and of Herwig (cluster model). 3000 ensemble tests have been performed. The results of the helicity fractions for the different showering algorithms are indicated in Tab 6.11.

	Pythia	Herwig	Difference
F_0	0.392 ± 0.003	0.483 ± 0.003	0.091
F_-	0.461 ± 0.002	0.419 ± 0.003	0.042
F_+	0.147 ± 0.002	0.098± 0.002	0.049

Table 6.11: Helicity fractions for the hadronisation with Pythia and Herwig. The right column contains the difference of the helicity fractions.

The difference of the fit results between the two Monte Carlo samples are taken as the systematic uncertainties. The results for a fixed right-handed fractions are shown in Tab. 6.12.

	Pythia	Herwig	Difference
F_0	0.6868 ± 0.0008	0.6801 ± 0.0009	0.0067
F_-	0.3131 ± 0.0008	0.3199 ± 0.0009	0.0068

Table 6.12: Helicity fractions for hadronisation with Pythia and Herwig with a fixed right-handed fraction.

6.5.7 W + Jet Normalisation

The dominant background process of the semileptonic $t\bar{t}$ decays are W + jets events. The background process has been investigated by Monte Carlo generators whereas the predictions depend on the renormalization scale. Therefore only a range for the background contribution can be quoted. The uncertainty due to the W+jets normalisation is investigated by scaling the W+jets processes by ± 20%. The background contributions are added to the pure signal and 5000 ensemble tests were performed, see Fig. 6.17. Again the procedure has been applied to a two-dimensional fit with a fixed right-handed fraction, see Fig. 6.18. The slope of the fitted functions indicates the systematic uncertainty.
Tab. 6.13 contains the uncertainties due to the W + jets background processes.

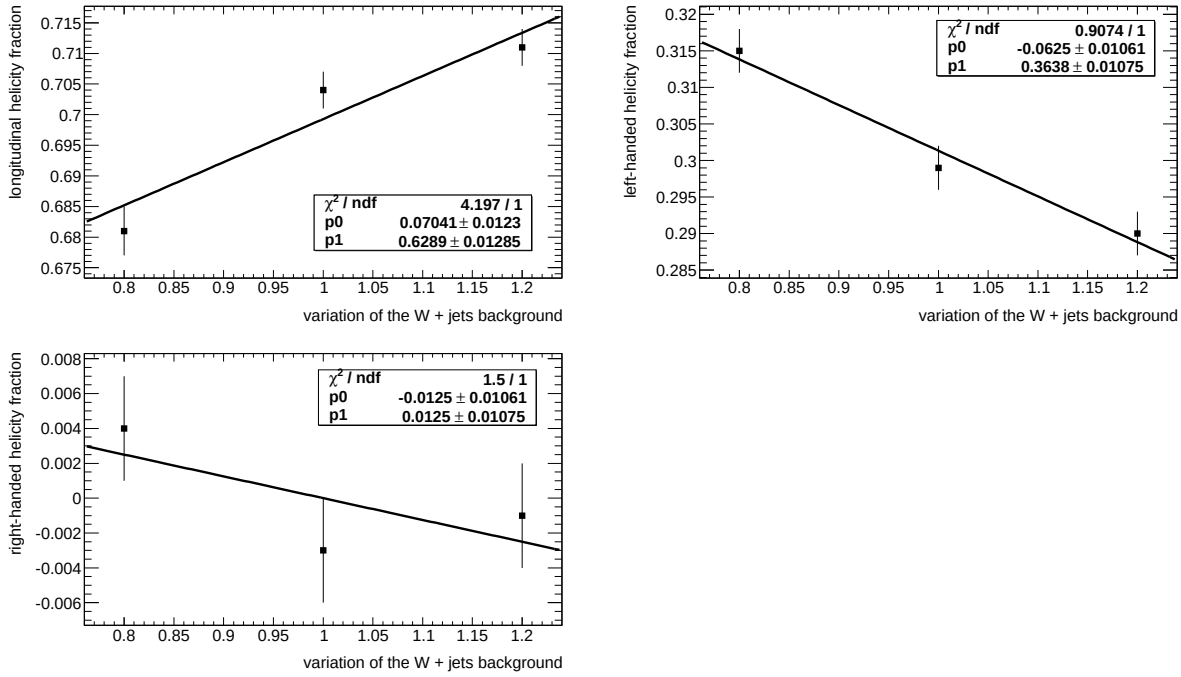

Figure 6.17: Helicity fractions as a function of the W+jets background contribution.

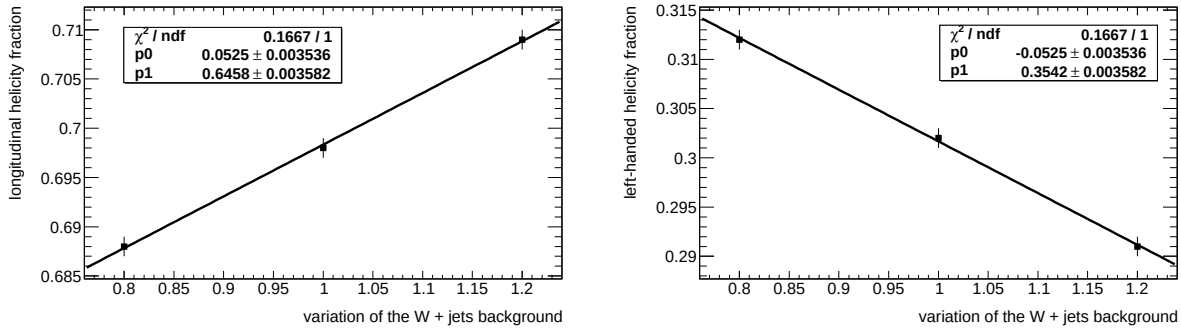

Figure 6.18: Helicity fractions as a function of the W+jets background contribution for the fixed right-handed fraction.

	F_+ included	F_+ fixed
F_0	0.014	0.011
F_-	0.013	0.011
F_+	0.003	-

Table 6.13: Summary of the systematic uncertainty for the three helicity states due to the uncertainty of W-normalisation.

6.5.8 Background Uncertainty

The knowledge of the background distribution is crucial for the analysis of the helicity fraction. The estimation of the background uncertainty is determined by scaling the non-W+jets background contribution by ± 10 %. The new background sample is scaled to the pure signal sample. The helicity fractions depending on the variation of the background very again fitted with a linear function. The parameters of the fit as a function of the three background contributions are shown in Fig. 6.19 and Fig. 6.20 for the fixed right-handed fraction. It can be seen that the linear behaviour is not a good approximation.

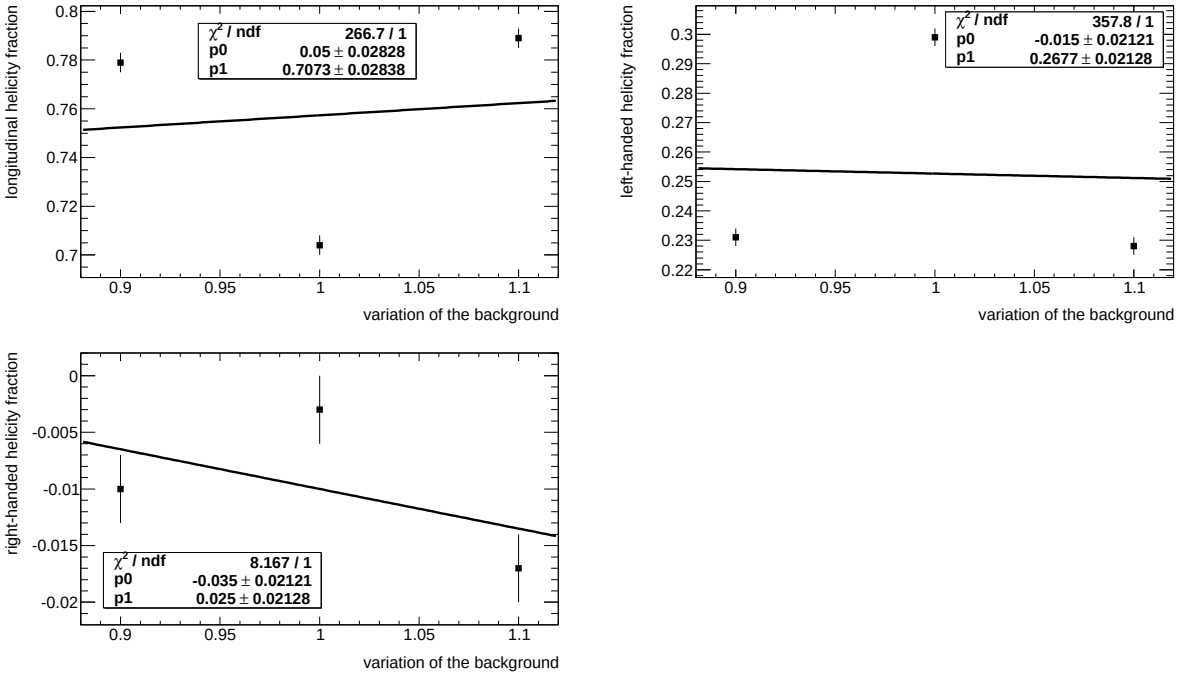

Figure 6.19: Helicity fractions as a function of the scaled non-W+jets background contribution by ± 10%. The value 1.1 corresponds to a up-scaling of 10 %.

The systematic uncertainties are extracted from the slope of the fitted function and summarised in Tab. 6.14.

6.5.9 PDF

The systematic uncertainty due to the parton density functions (see chapter 2.2.1) is evaluated for two different generators: CTEQ6 [36] and MRST. Due to the short time given in a Bachelor thesis, the PDF uncertainty has been evaluated by calculating the

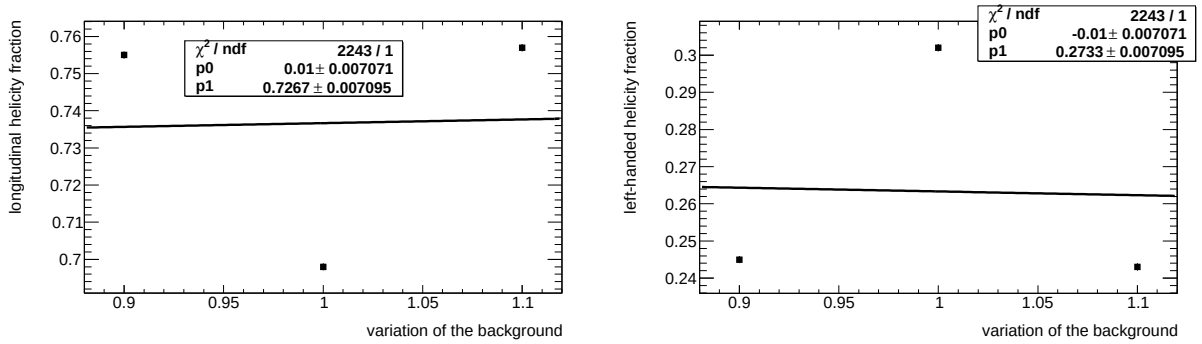

Figure 6.20: Helicity fractions as a function of the scaled background contribution by ± 10% for the fixed right-handed fraction.

	F_+ included	F_+ fixed
F_0	0.005	0.001
F_-	0.002	0.001
F_+	0.004	-

Table 6.14: Systematic uncertainties due to the background contributions.

difference of the helicity fractions between the two generators. The results are shown in Tab. 6.15 for the three dimensional fit and in Tab. 6.16 for the two dimensional fit. This method underestimates the uncertainties. For a complete analysis, the PDF systematics have to be evaluated via a reweighting scheme. The probability for each event with two hard partons, given flavour, momentum and energy transfer, has to be calculated. The uncertainty is then estimated by the difference of the error bands for the two PDFs from CTEQ6 and MRST.

	CTEQ	MRST	variation
F_0	0.619 ± 0.003	0.603 ± 0.003	0.016
F_-	0.380 ± 0.003	0.392 ± 0.003	0.012
F_+	0.001 ± 0.003	0.005± 0.003	0.004

Table 6.15: Helicity fractions for the two parton density function generators CTEQ and MRST and their difference.

	CTEQ	MRST	variation
F_0	0.622 ± 0.001	0.613 ± 0.001	0.009
F_-	0.378 ± 0.001	0.387 ± 0.001	0.009

Table 6.16: Helicity fractions for the two parton density function generators CTEQ and MRST for a two dimensional fit with a fixed right-handed fraction.

6.5.10 Pile-up

The systematic uncertainty due to the overlap of proton interactions from consecutive bunches, which are reconstructed as one event, is described by the pile-up. To determine the uncertainties, two samples were generated with MC@NLO. One nominal sample was produced and one sample with 4.1 pile-up collisions per event was produced. The difference of the helicity fractions between the two Monte-Carlo samples is taken as the systematic uncertainties. The fit results for the nominal sample and the sample with pile up effects is shown in Tab. 6.17. The study has been repeated with a fixed right-handed fraction, see Tab. 6.18.

	Pile-up sample	Nominal sample	Difference
F_0	0.678 ± 0.004	0.673 ± 0.004	0.005
F_-	0.307 ± 0.003	0.327 ± 0.004	0.020
F_+	0.015 ± 0.003	0.000± 0.003	0.015

Table 6.17: The impact of the pile-up on the helicity fractions.

	Pile-up	Nominal	Difference
F_0	0.709 ± 0.001	0.670 ± 0.001	0.039
F_-	0.291 ± 0.001	0.330 ± 0.001	0.009

Table 6.18: Helicity fractions from a two parameter fit under the influence of the pile-up.

6.5.11 Correlation Between Two Spin Analyser.

In order to estimate the correlation between the lepton p_T and $\cos\theta^*$, 3000 ensembles (pure signal) have been created with 3825 events each by taking random events out of the Protos SM sample and calculating the variables for these events. The distributions have been normalised to 200 pb^{-1}. The distributions have been fitted with the respective templates using Minuit and the fit results have been histogrammed. The fit results have been plotted in two dimensions using the fit results of both analysers for each ensemble. The spin analysers are obviously barely correlated. This allows to use the distributions for studies of multivariate analysis techniques, provided for example by the TMVA package.

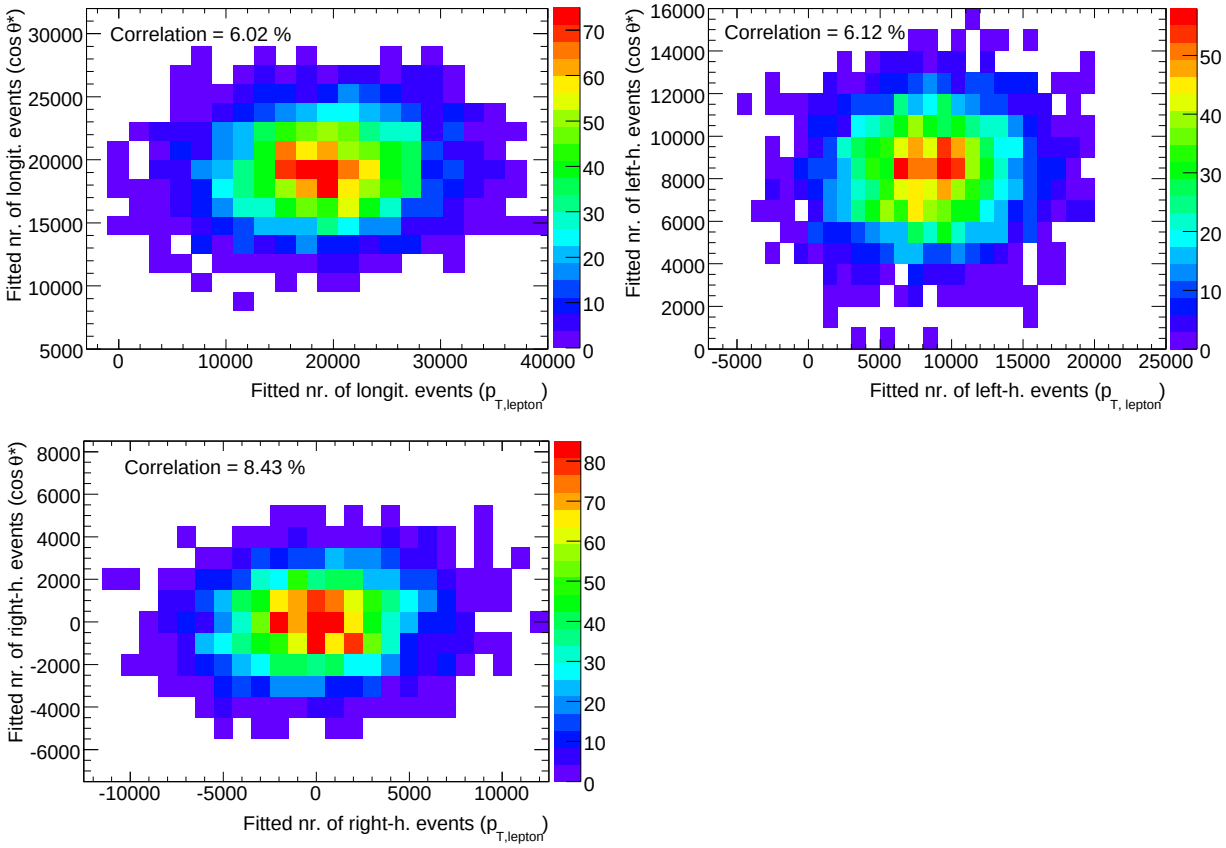

Figure 6.21: Correlation of the spin analysers $\cos\theta^*$ and p_T for the three different helicity states.

7 Conclusion

In the following, the results of the analysis are summarised and an outlook for further studies is given.

7.1 Summary

In this thesis, the helicity fraction of the W-boson have been analysed using the p_T of the charged electron. A template method has been applied to estimate the fractions from Monte Carlo data sets with a center-of-mass energy of 10 TeV. All studies have been performed for an integrated luminosity of $\mathcal{L} = 200$ pb^{-1}. Closure tests have been used to show the performance of the method. For fits including positive and negative parameters, the fractions can be estimated without a bias. For limiting the fit range to positive parameters only, the calibration curves show the expected bias. The statistical uncertainties have been estimated using signal and background events. The calibration curve showed that the fraction can be estimated without bias. For these ensemble tests, the data sets have been generated using Protos Monte Carlo only.

Furthermore, systematic uncertainties have been evaluated. Uncertainties on the Lepton Energy Scale lead to larger systematic uncertainties while the JES uncertainty is small as expected. The studies due to the systematic uncertainties also showed that a three parameter fit underestimates the longitudinal fraction while the right-handed fraction is overestimated. Therefore two dimensional fits were performed for comparison. Fixing the right-handed fraction results in smaller systematic uncertainties.
The uncertainty due to the top quark mass was expected to be small since the top mass was used as a free parameter with a Breit-Wigner constraint. This can also be seen in Tab. 7.1 and 7.2. For the three parameter fit, the largest contribution comes from the uncertainty of the Monte Carlo generator due to the large deviation of the

AcerMC sample. For the two parameter fit the total uncertainties are also mainly dominated by the result for the Monte Carlo Generators. Tab 7.1 and 7.2 summarise the systematic uncertainties for the fits with all three helicity states and for the fits with a fixed right-handed fraction. Furthermore the total systematic uncertainty for each helicity state is calculated. The total uncertainty for the helicity states are also quoted.

Table 7.1: Summary of the systematic and statistical uncertainties for the fit with three parameters.

Sample	F_0	F_-	F_+
Theoretical			
Top quark mass (2.5 GeV/c^2)	0.003	0.012	0.015
ISR/FSR	0.092	0.062	0.034
MC Generators	0.223	0.069	0.148
Fragmentation	0.091	0.042	0.049
W+jet normalisation (20%)	0.014	0.013	0.003
background (10%)	0.005	0.002	0.004
PDF	0.016	0.012	0.004
Experimental			
LES (1%)	0.078	0.027	0.054
JES (5%)	0.001	0.003	0.004
Pile-up (4.1)	0.005	0.020	0.015
Total systematic uncertainty	0.270	0.109	0.170
Statistical uncertainty with bkg.	0.270	0.250	0.175
Total uncertainty	0.382	0.273	0.244

Table 7.2: Summary of the systematic and statistical uncertainties for the fixed right-handed fraction.

Sample	F_0	F_-
Theoretical		
Top quark mass (2.5 GeV/c^2)	0.028	0.028
ISR/FSR	0.025	0.033
MC Generators	0.079	0.079
Fragmentation	0.0067	0.0068
W+jet normalisation (20%)	0.011	0.011
background (10%)	0.001	0.001
PDF	0.009	0.009
Experimental		
LES (1%)	0.030	0.029
JES (5%)	0.007	0.007
Pile-up (4.1)	0.039	0.009
Total systematic uncertainty	0.102	0.097
Statistical uncertainty with bkg.	0.199	0.134
Total systematic uncertainty	0.224	0.165

7.2 Outlook

To finalise these studies, also μ+jets events have to be taken into account. The two channels have to be properly combined taking into account correlations between both channels. Furthermore, a comparison with other spin analysers would be interesting. Besides it would also be interesting to repeat the studies with the dileptonic decay channel of $t\bar{t}$ events.

The results for the systematic uncertainties show for the three dimensional fit an underestimation of the longitudinal fraction, especially for the AcerMC samples. More effort is neccessary to understand the source of this effect.

To improve the performance of the study, b-tagging information could be used in order to reduce the combinatorial background. Due to the low correlation between the two analysers, the application of multivariate techniques like Artifical Neural Networks or Boosted Decision Trees could improve the classification of the events. This method has been successfully applied for cross section measurements.

While the LHC is collecting an increasing amount of integrated luminosity per week, the studies have to be repeated with 7 TeV Monte Carlo in order to set up the

machinery for the analysis of real data.

A Appendix

Table A.1: Summary of the samples used for the systematic uncertainties. The MC generator, the showering algorithm and the reconstruction algorithm is quoted.

Uncertainty	Sample	Generator	Showering	Reconstruction
LES + JES (SM)	105362	Protos	Pythia	Full Reco
LES + JES (F_+)	105363	Protos	Pythia	Full Reco
LES + JES (F_-)	105364	Protos	Pythia	Full Reco
LES + JES (F_0)	105365	Protos	Pythia	Full Reco
Top Mass (170 GeV/c^2)	106201	MCatNLO	Jimmy	ATLFast
Top Mass (180 GeV/c^2)	106202	MCatNLO	Jimmy	ATLFast
Top Mass (160 GeV/c^2)	106203	MCatNLO	Jimmy	ATLFast
MC Generators	105205	AcerMC	Herwig	Full Reco
MC Generators	105200	MCatNLO	Jimmy	Full Reco
ISR/FSR (Nom.)	105205	AcerMC	Pythia	ATLFast
ISR/FSR (Var.)	106260	AcerMC	Pythia	ATLFast
ISR/FSR (Var.)	106261	AcerMC	Pythia	ATLFast
Fragmentation	105205	AcerMC	Pythia	Full Reco
Fragmentation	105206	AcerMC	Herwig	Full Reco
Pileup (nom.)	105200	MCatNLO	Jimmy	Full Reco
Pileup (var.)	105200	MCatNLO	Jimmy	Full Reco
PDF (MRST 2001 E)	105200	MCatNLO	Jimmy	Full Reco
PDF (CTEQ6m)	105200	MCatNLO	Jimmy	Full Reco

Bibliography

[1] D. Griffiths, *Introduction to elementary particles*, Weinheim, Germany: Wiley-VCH (2008) 454 p.

[2] C. Amsler *et al.*, *Review of particle physics*, Phys. Lett. **B667**, 1 (2008).

[3] Tevatron Electroweak Working Group, *Combination of CDF and D0 Results on the Mass of the Top Quark Using up to 5.6 fb$^-$1 of Data*, (2010), arXiv:1007.3178v1 [hep-ex].

[4] F. Abe *et al.*, *Observation of top quark production in $\bar{p}p$ collisions*, Phys. Rev. Lett. **74**, 2626 (1995).

[5] S. Abachi *et al.*, *Observation of the top quark*, Phys. Rev. Lett. **74**, 2632 (1995).

[6] N. Kidonakis and R. Vogt, *The Theoretical top quark cross section at the Tevatron and the LHC*, Phys. Rev. **D78**, 074005 (2008).

[7] B. Acharya and P. Ferrari, *Prospects for measuring the Top Quark Pair Production Cross-section in the Single Lepton Channel at ATLAS in 10 TeV pp Collisions*, (2009), Atlas Note.

[8] W.-K. Tung, *New generation of parton distributions with uncertainties from global QCD analysis*, Acta Phys. Polon. **B33**, 2933 (2002), [hep-ph/0206114].

[9] T. Aaltonen *et al.*, *First Observation of Electroweak Single Top Quark Production*, Phys. Rev. Lett. **103**, 092002 (2009).

[10] V. M. Abazov *et al.*, *Observation of Single Top-Quark Production*, Phys. Rev. Lett. **103**, 092001 (2009), arXiv:0903.0850 [hep-ex].

[11] M. Mohammadi Najafabadi, *Single top production at LHC*, (2006), [hep-ex/0605034].

[12] N. Kidonakis, *Single top quark production cross section at hadron colliders*, (2010), arXiv:1005.3330v1 [hep-ph].

[13] J. M. Campbell, R. Frederix, F. Maltoni, and F. Tramontano, *NLO predictions for t-channel production of single top and fourth generation quarks at hadron colliders*, JHEP **10**, 042 (2009).

[14] T. M. Liss and A. Quadt, *The Top Quark*, J. Phys. **G 37**, 075021 (2010), K. Nakamura *et. al* (Particle Data Group).

[15] W. Bernreuther, *Top quark physics at the LHC*, J. Phys. **G35**, 083001 (2008), arXiv:0805.1333 [hep-ph].

[16] I. I. Bigi, Y. L. Dokshitzer, A. Khoze, J. H. Kuhn, and P. M. Zerwas, *Production and Decay Properties of Ultraheavy Quarks*, Phys. Lett B **181**, 157 (1986).

[17] A. Ceccucci, Z. Ligeti, and Y. Sakai, *The CKM quark-mixing matrix*, J. Phys. **G 37**, 075021 (2010), K. Nakamura *et. al* (Particle Data Group).

[18] A. Quadt, *Top quark physics at hadron colliders*, Eur. Phys. J. **C48**, 835 (2006).

[19] M. W. Grünewald and A. Gurtu, *The mass and width of the W boson*, J. Phys. **G 37**, 075021 (2010), K. Nakamura *et. al* (Particle Data Group).

[20] M. Fischer, S. Groote, J. G. Korner, and M. C. Mauser, *Longitudinal, transverse plus and transverse minus W bosons in unpolarized top quark decays at O(α(s))*, Phys. Rev. **D63**, 031501 (2001), arXiv:0011075 [hep-ph].

[21] V. M. Abazov *et al.*, *Model-independent measurement of the W boson helicity in top quark decays at D0*, Phys. Rev. Lett. **100**, 062004 (2008).

[22] C. Collaboration, *Measurement of W Boson Helicity Fractions in Top Quark Decay to Lepton+Jets Events using a Matrix Element Analysis Technique with 1.9 fb^{-1} of Data*, (2007), CDF note 9144.

[23] A. Abulencia *et al.*, *Measurement of the helicity of W bosons in top-quark decays*, Phys. Rev. **D73**, 111103 (2006).

[24] http://public.web.cern.ch/public/en/Research/AccelComplex-en.html.

[25] M. Benedikt, (Ed.), P. Collier, (Ed.), V. Mertens, (Ed.), J. Poole, (Ed.), and K. Schindl, (Ed.), *LHC Design Report. 3. The LHC injector chain*, CERN-2004-003-V-3.

[26] O. S. Bruning, (Ed.) *et al.*, *LHC design report. Vol. I: The LHC main ring*, CERN-2004-003-V-1.

[27] G. Aad *et al.*, *The ATLAS Experiment at the CERN Large Hadron Collider*, JINST **3**, S08003 (2008).

[28] G. Aad *et al.*, *Expected Performance of the ATLAS Experiment - Detector, Trigger and Physics*, (2009), arXiv:0901.0512 [hep-ex].

[29] J. Aguilar-Saavedra, www-ftae.ugr.es/protos/manual.ps.

[30] S. Agostinelli *et al.*, *GEANT4: A simulation toolkit*, Nucl. Instrum. Meth. **A506**, 250 (2003).

[31] M. L. Mangano, M. Moretti, F. Piccinini, R. Pittau, and A. D. Polosa, *ALPGEN, a generator for hard multiparton processes in hadronic collisions*, JHEP **07**, 001 (2003).

[32] B. P. Kersevan and E. Richter-Was, *The Monte Carlo event generator AcerMC version 3.5 with interfaces to PYTHIA 6.4, HERWIG 6.5 and ARIADNE 4.1*, (2008).

[33] S. Frixione and B. R. Webber, *Matching NLO QCD computations and parton shower simulations*, JHEP **06**, 029 (2002).

[34] J. Erdmann, K. Kröninger, O. Nackenhorst, and A. Quadt, *Kinematic fitting of $t\bar{t}$ events using a likelihood approach - The KLFitter package*, (2009), ATL-COM-PHYS-2009-551.

[35] A. C. Caldwell, D. Kollar, and K. Kroninger, *BAT: The Bayesian analysis toolkit*, J. Phys. Conf. Ser. **219**, 032013 (2010), 17th International Conference on Computing in High Energy and Nuclear Physics (CHEP09).

[36] http://www.phys.psu.edu/ cteq.

[37] G. Cowan, *Statistical data analysis*, Oxford, UK: Clarendon (1998) 197 p.

[38] K. Kröninger, *Estimating contributions from different processes – A Bayesian approach to the template method*, (2010), ATL-COM-PHYS-2010-186.

Acknowledgements

First of all I would like to thank Andrea Knue who supervised me during the past few months. It was a pleasure for me to share the office with her and I am very grateful for her patience concerning my questions. Special thanks for bringing me breakfast after a long night writing this thesis. I couldn't have wished for a better supervisor.
Moreover I would like to thank Kevin Kröninger for his supervision. He always had constructive suggestions and helped reviewing this thesis
Special thanks go to my first referee Prof. Dr. Arnulf Quadt who prodded me to write my Bachelor's thesis in the high energy physics. Futhermore I would like to thank him for giving me the opportunity to participate in the summer student programm @ DESY. I also would like to thank Prof. Dr. Ariane Frey for being the second referee.
Furthermore I want to thank my family and friends for their support and encourage during the past few month.

Erklärung nach §13(8) der Prüfungsordnung fr̈ den Bachelor-Studiengang Physik und den Master-Studiengang Physik an der Universität Göttingen:

Hiermit erkläre ich, dass ich diese Abschlussarbeit selbständig verfasst habe, keine anderen als die angegebenen Quellen und Hilfsmittel benutzt habe und alle Stellen, die wr̈tlich oder sinngemäß aus veröffentlichten Schriften entnommen wurden, als solche kenntlich gemacht habe.
Darüberhinaus erkläre ich, dass diese Abschlussarbeit nicht, auch nicht auszugsweise, im Rahmen einer nichtbestandenen Prüfung an dieser oder einer anderen Hochschule eingereicht wurde.

Göttingen, den December 2, 2010

(Chris Malena Delitzsch)